LUND UNIVERSITY
Faculty of Science

Investigating Optical-Field-Induced Currents in GaN using Ultrafast Lasers

Vidar Flodgren

Thesis submitted for the degree of Master of Nanoscience

Project Duration: 1 Year

Supervisor: Anders Mikkelsen
Co-Supervisor: Fabian Langer

Department of Physics
Division of Synchrotron Radiation Physics

May 2019

Contents

Abbreviations and Definitions

BP	-	Banana Plug
BNC	-	Bayonet Neill-Concelman
CEP	-	Carrier Envelope Phase
EBL	-	Electron Beam Lithography
FWHM	-	Full Width at Half Maximum
GPIB	-	General Purpose Interface Bus
GVD	-	Group Velocity Dispersion
JC	-	Jumper Cable
IV	-	Current-Voltage
IPA	-	Isopropyl Alcohol
OBE	-	Optical Bloch Equation
Ti:Sa	-	Titanium:Sapphire
Yb	-	Ytterbium
Ti/Au	-	Titanium/Gold
TOD	-	Third Order Dispersion

Acknowledgements

First and foremost, I'd like to extend thanks to my supervisor, Anders Mikkelsen, for offering me the wonderful opportunity to work on such a multifaceted and interesting project, in addition to providing me with valuable guidance and insight over the course of the project.

To Fabian Langer, my co-supervisor, I'd like to express my thanks for the theoretical and experimental guidance, for answering all of the theory questions I've thrown your way, for instructing me in the lab, and especially for taking the extra time to gather some more data for the final version of my thesis.

I'd like to also thank Yen-Po, for fabricating the first few test devices that we used in experiments. But not only for that, but also for enduring the arduous process of teaching me how to use the wire bonder, and for instructing me on how to use the AVAC system.

Finally, I'd like to thank Zhe-Ren for running me through the different fabrication processes on multiple occasions, especially for taking the time out of your schedule on such short notice to give me a hand when I needed it.

Working in a research group environment has been a highly positive experience for me, and I'm very happy to have been allowed to take part in the research within it. For that, I'd like to thank you all again for making it all possible.

Abstract

This study saw the development of an experimental setup capable of generating and measuring optical-field-induced currents in a variety of nanodevices fabricated specifically for this project. Each device design features two metallic contacts, closely separated by about 5 µm, deposited onto a semiconductor or insulator substrate. The region between these two contacts is a junction, being where the laser is focused to generate, and consequently measure, the current. In total, 15 separate substrate samples had nanodevices fabricated onto them. Most devices were made using gold etching, placing Au on mostly GaN substrates, but some SiC and SiO_2 substrates were also used. Devices were also fabricated using a lift-off procedure, allowing for a Ti/Au-GaN device to be made.

Two separate laser systems were used to investigate the generation of optical-field-induced currents. One, a titanium-sapphire laser generating a field asymmetry by ultrashort pulses, the other a ytterbium laser generating it by a fundamental and second harmonic superposition. However, while currents were measured with both laser systems, several characteristics of the signal raised further questions. The phase modulation of the Ti:Sa laser did not result in a current oscillation, nor did the device only produce a current when the pulse was polarised in the direction of the junction, instead generating a current even with a perpendicularly polarised pulse. On the other hand, the Yb laser measurements seemed to confirm that the current direction has a polarisation dependence, since no current was generated with perpendicularly polarised pulses, and when reversing the polarisation there was a sign change in the current. However, modulating the relative delay of the two pulses from the Yb laser generated no current oscillation, unlike what was expected from the model. Furthermore, the high intensities required to induce a current would ablate both the gold and substrate materials, destroying the devices. Likewise, the phase modulation of the Ti:Sa also saw no change in current.

To substantiate the experimental efforts, a model derived from Bloch equations developed by Khurgin[1] to estimate the photoinduced charge produced by a single, or two cross-polarised, laser pulses on a device was recreated. It was also expanded upon to cover two-colour experiments, like the wave superposition used in the Yb laser experiments. Finally, a fully featured GUI was written to more easily control the parameters of the model, having the potential to quickly create and compare experimental results to the expected modelled outcome.

1 Introduction

For the past 30 years, much research has been done to determine the mechanisms that lead to laser-induced currents being generated in dielectric materials exposed to strong optical fields. Early experiments focused solely on the generation through the coherent control of two-colour incident laser radiation on both semiconductor and insulator materials, mainly on gallium arsenide (GaAs).[2–8] In these experiments, one of the pulses is resonant an initial state, and the other one can induce two-photon absorption into a given final state. The intensities of these laser pulses are then tuned until they create similar carrier concentrations, where the resulting interference produces an asymmetric distribution in k-space, leading to a directed and measurable current.

However, with the emergence of laser systems capable of generating temporally asymmetric pulses, consisting of only a few optical cycles, it was discovered that the same devices on wide bandgap semiconductors, like silicon dioxide (SiO_2) and gallium nitride (GaN), could have so-called optical-field-induced current induced using only a single colour laser,[1, 9–13] sometimes also introducing an additional orthogonally polarised injection pulse to decouple the driving and injection processes.[1, 9, 10] One of the main driving forces behind this research comes from the prospect of utilising this phenomenon in devices that have much higher response times than conventional electronics, not only enabling GHz operation of photodetectors,[14] but also allowing for the development of complex biosensors and transparent electrodes.[15] Since the current response would be the only determining factor in detection, this also carries the advantage of allowing for the direct determination of both the phase of incident light pulses, as well as the field-waveform.

One goal of this thesis is to attempt to reproduce the conditions and apparatus used in the studies by Schiffrin[9] and Paasch-Colberg et al.[10] in order to measure, and evaluate the causes for, the optical-field-induced currents in GaN nanodevices when exposed to ultrashort pulses from a singly polarised laser. This will not only include the apparatus construction, but also the fabrication of suitable devices whose architecture supports the phenomenon. In addition to this, another goal was to write the code for a complementary model whose purpose is to estimate the photoinduced charge per incident pulse in order to compare experimental results to the model.

The aim is therefore to attempt to form a deeper understanding of the underlying cause and, consequently, process by which optical-field-induced currents emerge in diffe-

rent semiconductor and insulator materials when exposed to strong optical fields delivered through ultrashort laser pulses.

2 Background and Theory

Over the years, there has been a significant amount of discussion surrounding the fundamental mechanisms by which optical-field-induced current emerge in both semiconductor and insulator materials, both in single and two-colour experiments. The phenomenon itself has been experimentally observed in a wide variety of substrates, from insulator materials like SiO_2 [9, 11, 16] to wide bandgap semiconductors, like GaN [10, 17] and GaAs, [3–6, 8] as well as in few monolayer structures like Graphene. [18, 19] These studies have generated many varying interpretations of the phenomenon.

2.1 A Summary of Proposed Models

The underlying mechanism that explains how currents can be induced by the introduction of a strong optical field is not yet fully understood, and as such there exist several different theoretical models that propose various ideas on how these optical-field-induced currents arise in wide bandgap insulator and semiconductor materials. This section will give a brief outline of four currently proposed theoretical explanations of the phenomenon.

The first proposal, made by I. Franco et al. [13] in a study focusing on the ultrafast current generation in molecular wires, utilises a two frequency laser incidence (ω,2ω) system to induce temporal asymmetry of the pulses. The study attributes the current generation to Wannier-Stark localization and Stark shifts, something that many of the other studies concluded also. When a lattice is exposed to a strong field, the continuous states of the field-free band structure split up into so-called Wannier stark states, localised at atomic sites in the lattice. Their energy separation is defined by the Bloch energy, and they permit electrons to hop from one lattice site to another with a lower eigenstate energy. This can only happen if the Fermi level aligns with a free Wannier stark state, where electron transport can only propagate if there are additional free states above its Fermi level. Thus, the electron transport occurs by the shifting of the Fermi level by the incident laser, allowing electrons to flow from occupied states to unoccupied ones.

The second comes from a study by Shiffrin et al, [9, 20] proposing that exposing a dielectric material substrate to ultrashort laser pulses with a strong optical field effectively

transforms the material into a state of high polarisability. From this state, localised optical-field-induced currents can arise, allowing the carriers to flow in the direction of the incident singly polarised laser pulse. The theoretical explanation given for the field induced state of increased polarisability comes as a result of the dynamic formation of Wannier-Stark states. In essence, it is the adiabatic crossing of the valence with the conduction band which allows for a strong transition from a valence band state to an unoccupied state, increasing the polarisability, and thus allowing for interband Zener tunnelling to occur at high injection field strengths.

Kruchinin et al. expand further on the research by Schiffrin et al. suggesting instead a more conventional approach. This third proposal focuses mainly on the interference between different multiphoton excitation pathways.[21] Parallels are drawn with results gained from studies done on the coherent control of two overlapping laser pulses that generate currents by one or two-photon excitation in semiconductor materials.[2,4,5] The model argues that the resultant optical-field-induced currents generated by pulse overlap can be evaluated from the solution of multiband optical Bloch equations combined with the solution for the dielectric equations of polarisation in the crystal. The model found that, at low field intensities, the greatest charge contributions should come from the interference between the 5 and 6 photon channels.

Finally, a fourth interpretation comes from Jacob B. Khurgin,[1] whose theory be referenced in more detail in this paper. The study proposes that the current emerges as a result of virtual carrier generation in both valence and conduction bands by multiphoton quantum interference. The study concluded that the majority contribution to the current was in the quantum interference of one and two-photon transitions, or two and three-photon transitions.

A study by L. Chen et al.[22] used atomistically resolved quantum transport simulations to attempt to determine the mechanism by which currents propagate. They also briefly evaluate each of the proposed four models. The results from this simulation heavily suggest that neither Wannier-Stark metallisation nor Zener interband tunelling are required for optical-field-induced currents to arise. Furthermore, it is suggested that generating real carriers in resontant 5 and 6 photon channel absorption cannot be confirmed from the experimental observations from coherent control. Further research needs to be done in order to determine the mechanism that optical-field-induced currents are generated by.

2.2 Multiphoton Excitation and Quantum Interference

To avoid most resonant effects, the driving laser pulse must have an energy lower than the band gap transition energy E_g, meaning that no real carriers can be generated by a direct transition. On the other hand, virtual carriers, creating a polarisation of the medium, may still be excited through a multiphoton process. Note, however, that this does not prevent a resonant multiphoton excitation of real carriers into the conduction band. For instance, the two-photon process involves the excitation of an electron in the valence band into an intermediate virtual state, from which an additional excitation from another incident photon (of the same energy) allows the electron to be excited into the conduction band. Note, however, that this successive photoexcitation process is not stepwise, all steps should be assumed to take place simultaneously. As such, if the photon energy of the laser is $\hbar\omega$ and the bandgap is less than $2\hbar\omega$, then a two, or more, photon photoexcitation is possible. The most important thing to consider here is the fact that, even when a two-photon event is enough to excite an electron into the conduction band, a three-photon excitation can still occur. In that case, the electron is instead excited into the higher lying states of conduction band. These non-resonant excitations give rise to what is known as virtual carriers, since there are no energy states to support the excitation. They can otherwise be considered a polarisation of the medium.

If only individual multiphoton transitions are considered, then the expectation is that the generation of virtual carriers should produce no current, since an equal distribution of electrons should be generated with both positive and negative k-vectors because the magnitude of the dipole element is symmetric around k=0. However, with the presence of an electric field, a phenomenon known as quantum interference means that the excitation pathways of odd and even numbered photon transitions interfere with one another, generating an uneven population of virtual carriers with different sign k-vectors. Kruchinin et al.[21] provide a reason for this discrepancy when calculating the band structure, and plotting the later calculated diagonal matrix elements of the momentum operator $P_{ii} \equiv \hbar k + p_{ii}(k)$, where $p_{ii}(k)$ are the momentum matrix elements, and where i either represents the elements of the topmost valence band as v, or the lowermost conduction band as c. When this is plotted against A, demonstrated in Figure 1 (a), the two-photon

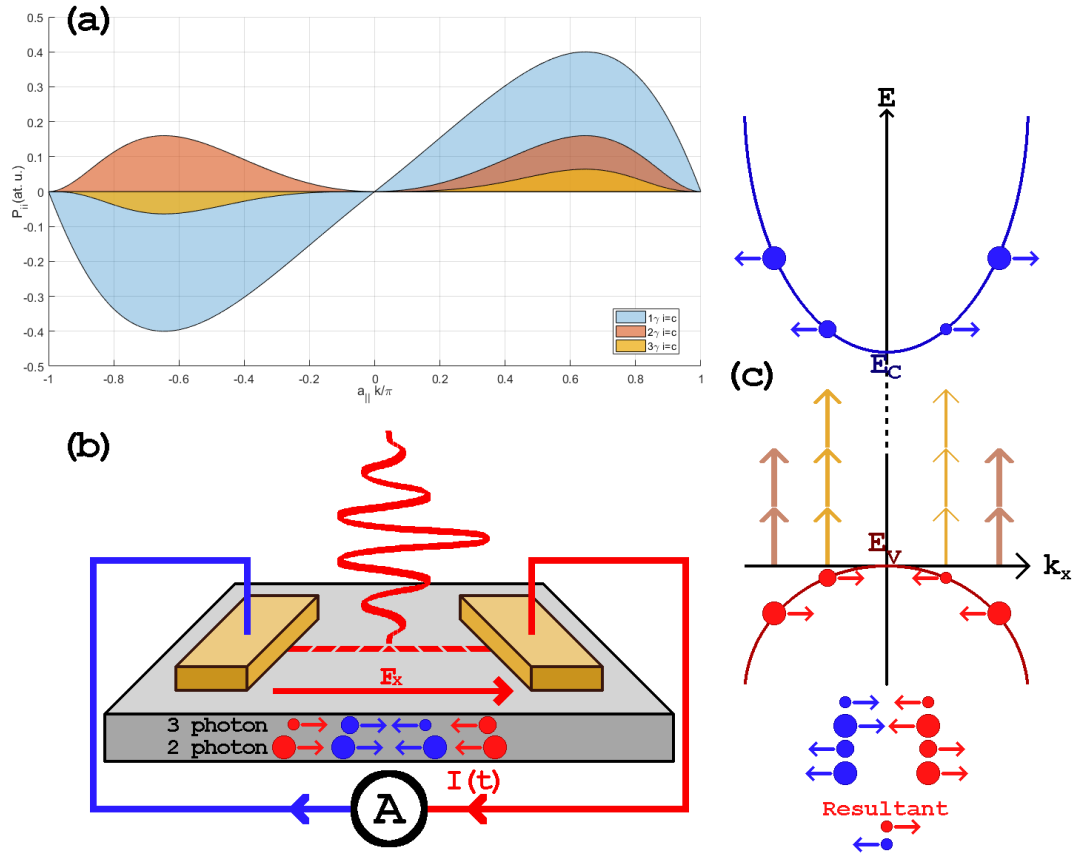

Figure 1: Three graphics summarising odd numbered photon excitation pathways generate nonzero currents. Panel (a) is a modified version of FIG. 2. b. from the paper by Kruchinin et al.[21] showing the diagonal matrix elements of the momentum operator for the lowermost conduction bands for one, two and three-photon excitation pathways. Panel (b) illustrates the relation between the direction of an optical field F_x and the resultant current generated by one and two-photon excitation pathways, showing virtual holes and electrons as red and blue circles respectively. Panel (c) shows the difference in the proportion of excitations to generate virtual carriers of the different signed particles in the conduction and valence bands, showing also the total resultant current from both excitation pathways. Panels (b) and (c) were created with reference to Fig. 1. a. of the paper by Khurgin.[1]

$P_{ii}(at.u.)$ when $i = c$ has positive values for both positive and negative k-vectors.

The multiphoton transition from the valence to the conduction band is mediated by the dipole matrix element, $d = d(k)$, which thus changes sign with the wave vector k. If the field is then introduced as E, expressed in the positive k direction, then the transition amplitude of any multiphoton transition with n number of photons can be denoted $(dE)^n$. Thus, any multiphoton transition with a positive k vector will have a positive transition amplitude $(dE)^n$, but the sign of this amplitude diverges for odd and even numbered transition pathways for negative k-vectors. Here, odd numbered transitions

give $(-dE)^{2n+1} = -dE^{2n+1}$, and even ones give $(-dE)^{2n} = dE^{2n}$. When this divergence is considered when solving the Hamiltonian, then there will be constructive interference for the transitions with positive k-vectors, and destructive interference for those with negative ones. This means that the total contributions to the current is greater from positive sign k-vector transitions than from negative sign k-vectors, as is also shown in the figure. Note also that $P_{ii}(at.u.)$ from $i = v$ follows the same trend, but mirrored in the x-axis, as the ones from $i = c$, but at about a tenth of the magnitude.[21] Figure 1 contains a full picture of the process by which the directional current arises from the interference between the 2 and 3 photon excitation pathways as a result of the incident laser pulse, with reference to a simplified version of the device.

The resultant current is therefore caused by the interference between even and odd numbered transitions, specifically between the $2n$ and $2n+1$ photon excitation pathways, where n is the number of photons transitions. As a consequence, since the direction of the incident field is what determines in which direction the generated carriers polarise the medium, it should be noted that the generated current will always follow the optical field. Thus, it should be possible to draw up a model that estimates the total resultant charge generated by the incidence of a single pulse, where the expected current can be estimated from the repetition rate, which is a description of the number of pulses incident to the sample per second.

2.3 A Model for Optical-Field-Induced Current

As discussed in Section 2.1, there are four different interpretations of how optical-field-induced currents are generated in wide bandgap semiconductors. This study will focus on the model created by Jacob B. Khurgin,[1] because, not only does the model provide an elegant and simple way to simulate the experiment, but it is rooted among the photoinjection experiments with coherent control of w-2w transitions, which are connected to the experiments that this study aims to do which have been shown to be connected to the experiments we want to do. As such, it is important to cover the relevant theory required to reproduce such a model.

2.3.1 A Mathematical Description of Laser Pulses

For this model, it is important that a laser pulse can be defined in both temporal and frequency space. In temporal space, propagating electromagnetic waves can be described using Maxwell's equations in vacuum conditions, namely

$$\nabla \cdot \bar{E} = 0 \quad (1) \qquad \nabla \cdot \bar{B} = 0 \quad (3)$$

$$\nabla \times \bar{E} = -\dot{\bar{B}} \quad (2) \qquad \nabla \times \bar{B} = -\mu\varepsilon\dot{\bar{E}}, \quad (4)$$

where ∇ is the gradient operator, $\bar{E}$ is the electric field, $\bar{B}$ is the magnetic field, μ is the permeability and ε the permittivity. From these, the wave equation of a single laser pulse in 3D space can be found. This is done by deriving the four Maxwell equations into a Helmholtz equation, a second order partial differential equation of the form $(\nabla^2 + k^2)A = 0$. This is done by taking the curl of Equation (4) and applying the vector identity $\nabla \times (\nabla \times A) = \nabla(\nabla \cdot A) - \nabla^2 A$, then substituting Equation (1) and the first order time derivative of Equation (4) into the left and right sides respectively, giving

$$\nabla(\underbrace{\nabla \cdot \bar{E}}_{\text{Eq}(1)\,=\,0}) - \nabla^2\bar{E} = \underbrace{\nabla \times \dot{\bar{B}}}_{\text{Eq}\frac{\partial}{\partial t}(4) = -\mu\varepsilon\ddot{E}} \Rightarrow \nabla^2\bar{E} - \mu\varepsilon\ddot{\bar{E}} = 0 \quad (5)$$

which can clearly be reduced to the form $(\nabla^2 - \mu\varepsilon\frac{\partial^2}{\partial t^2})\{B(\bar{r},t) \wedge E(\bar{r},t)\}$.[23] With this, the solution for the Helmholtz equation for the electric field is given by plane waves

$$\bar{E}(\bar{r},t) = \bar{E}_0 e^{-i(\omega t - \bar{k}\cdot\bar{r} + \phi_0)} \quad (6)$$

Since the field intensity is independent of the radial coordinate $\bar{r}$, which defines the 3D aspect of a propagating wave, this equation can be simplified to

$$\bar{E}(t) = \bar{E}_0 e^{-i(\omega t + \theta(t))}. \quad (7)$$

Using Euler's theorem, where $e^{-ix} = \cos(x) - i\sin(x)$, if setting $x = \omega t + \theta(t)$ then the wave can also be expressed using trigonometric functions instead, such that

$$Re(\bar{E}(t)) = \bar{E}_0 \cos\left(wt - \theta(t)\right). \quad (8)$$

A laser pulse can be described as the dot product of the plane wave described and an envelope function. This makes the modelling of such a pulse using computer software quite simple. The model would see the per-element-multiplication of two vectors of equal

length defined in the same temporal axis t, one describing the cosine function and the other the envelope. When modelling, it is important to centre the axis around which a plot is made, as such t can be replaced by $t - t_0$, which will place the centre of symmetry at $t - t_0 = 0$ when calculating.

The optical laser pulse envelope is usually referred to as the intensity envelope, defined as

$$I(t) = I_t e^{4\ln(2)\left(\frac{t-t_0}{T}\right)^2}, \text{ [24]} \tag{9}$$

and is a simple Gaussian. Here, I_t is the amplitude in temporal space (for a normalised envelope, it is equal to one), t is the time axis, t_0 is the time at which the pulse is centred (in this model, it is set to be the median of t), and T is known as the pulse duration. T, which is also defined as

$$T = \frac{2\pi N_{cyc}}{\omega_0}, \tag{10}$$

is also the full width at half maximum (FWHM) of the Gaussian. In this equation, ω_0 is the central frequency of the laser, and N_{cyc} is the number of optical cycles, detailing specifically how many oscillations take place within this FWHM. From a modelling perspective, it is far more useful to define T from N_{cyc}, since then the number of oscillations within the FWHM for any frequency ω_0 is already known.

However, the intensity envelope describes only the temporal energy distribution of the pulse, not the resultant electric field amplitude, which will be used to estimate the photoinduced charge generated. Consequently, the complex electric field amplitude $E(t)$ must then be calculated using the intensity envelope $I(t)$.[1,24]

$$E(t) = \underbrace{\sqrt{I_t e^{-4\ln(2)\left(\frac{t-t_0}{T}\right)^2}}}_{\sqrt{I(t)}} e^{-i(\overbrace{w_0(t-t_0)}^{\text{Oscillation}} + \overbrace{\theta(t)}^{\text{Phase}})} \tag{11}$$

$$E(t) = A_t e^{-2\ln(2)\left(\frac{t-t_0}{T}\right)^2} e^{-i(w_0(t-t_0)+\theta(t))} \tag{12}$$

Here, it should be noted that the temporal phase function $\theta(t)$, labelled as "Phase" in the equation, is a constant in most model. Using the complex electric field amplitude instead of the actual electric field $\mathscr{E}(t)$, otherwise given by

$$\mathscr{E}(t) = \frac{1}{2}E(t) + c.c. \tag{13}$$

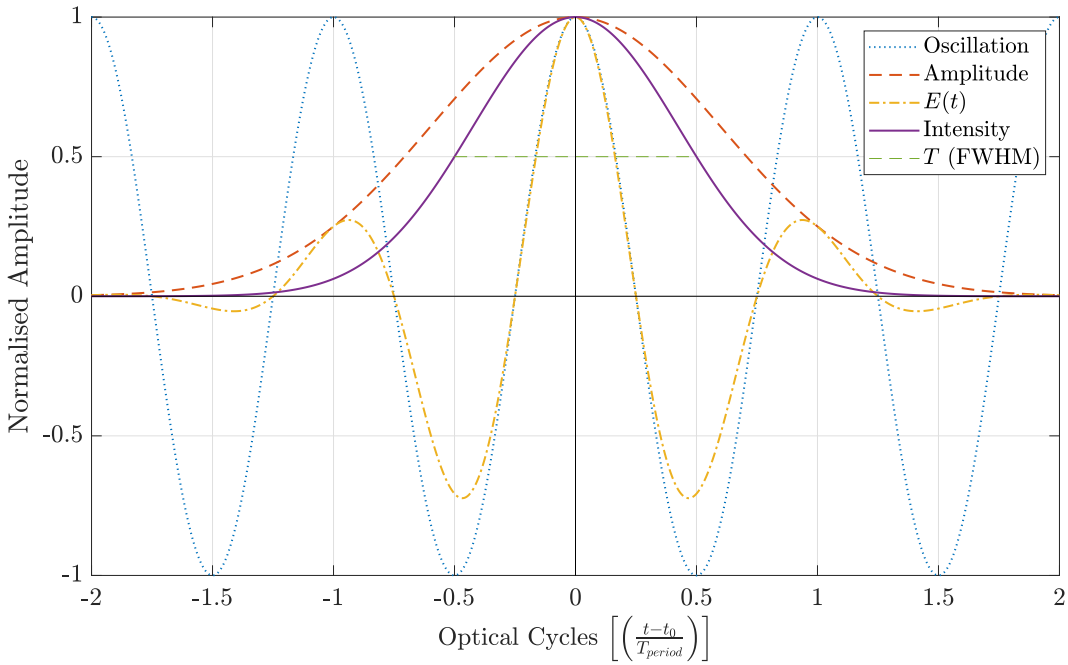

Figure 2: A graph plotted using Equation (12), showing only the real values represented in Equation (8), displaying the Amplitude and Oscillation components whose dot product gives the Electric pulse field $E(t)$. The Intensity envelope and T, the FWHM, are also shown. This was plotted using $N_{cyc} = 1$, as is evident by only a single oscillation being completed within the FWHM.

is advantageous as it makes calculations easier.[24] In the model, however, this means that all of the peak amplitudes are set so that $A_t = 1$ so that the vector potential is acquired instead of E_t. As a consequence, when calculating $E(t)$ using Equation (12), all values will be complex doubles. Even though all calculations are done using these complex numbers, when plotting any result graphically, as is in Figure 2, then only the real part needs to be considered, as should be evident from the simplification done in Equation (8), as well as physical reasons. The temporal phase function $\theta(t)$ is a constant, defining the temporal relationship between the frequency spectrum components.[25] This means that it is possible to simply let $\theta(t) = 0$. On the other hand, when multiple different laser pulses interact, it is important to have this defined for each, since it will influence the resultant field. Equation (8) therefore shows the real-valued observables of the electric pulse field, but Equation (12) will be used to evaluate the pulses in the model, opting instead to only graph the real part. Figure 2 shows a comprehensive summary of the mathematical process of defining and plotting the electric pulse field. These fundamentals give a basis for the next models that aim to show how laser pulses interact with various materials, and to

assist in identifying and verifying matching experimental results from similar conditions.

2.3.2 Modelling Dispersion

When dealing with real laser radiation, since the phase and delay are usually controlled using a pair of crystal wedges with variable thickness L, a material dependent effect known as dispersion must be taken into consideration for the distance through this material the laser travels. This dispersion, however, cannot be applied in temporal domain, but must instead be applied in frequency space using a dispersion factor, normally written as $e^{\Phi(\omega-\omega_0)}$. So, while Equation (12) shows the temporal domain of a laser pulse, the following shows instead the frequency domain equivalent.

$$E(\omega) = \underbrace{\sqrt{I_\omega e^{-\ln(2)\left(\frac{2(\omega-\omega_0)}{W}\right)^2}}}_{\text{Gaussian Envelope}} \underbrace{e^{-i\Phi(\omega-\omega_0)}}_{\text{Dispersion Factor}} \tag{14}$$

Here, I_ω could be considered the frequency domain intensity distribution, effectively describing the spectral energy distribution of the pulse. Integrating the frequency domain pulse gives the total energy of the pulse. Just as T is the FWHM of the intensity envelope, W is the FWHM of the equivalent envelope in frequency space. Defining them gives the following equations,

$$T = \frac{2\pi N_{cyc}}{\omega_0} \qquad W = \frac{4\ln(2)}{T}, \tag{15}$$

and by multiplying them together, giving

$$\Rightarrow TW = \frac{8\pi\ln(2)N_{cyc}}{\omega_0 \frac{2\pi N_{cyc}}{\omega_0}} = 4\ln(2), \tag{16}$$

it becomes evident that they are related by the uncertainty relation.[25,26] This has an impact on the model, since the higher the resolution chosen for time domain, the worse it will be when Fourier-transformed into frequency space.

The variable $\Phi(\omega-\omega_0)$ represents the terms of an n'th order Taylor expansion of the frequency dependent wavenumber $k(\omega)$ around the centre frequency ω_0. Knowing that $k = 2\pi\lambda_0$, it can be rewritten to be dependent on the refractive index n such that $k(\omega) = \frac{n(\omega)\omega}{c}$.[27] Thus, since the spatial phase factor $\phi = kL$ where L is the propagation length,

Table 1: A table detailing the observed effects that each ϕ_n component applied in the frequency domain has on the time domain pulse. Figure 3 shows an example of the resulting waves for each of these effects

ϕ_0	-	Alters the phase of oscillating components, does not alter pulse length.
ϕ_1	-	Shifts the pulse envelope in time, does not alter pulse length
ϕ_2	-	Linearly alters the instantaneous frequency ω_i and stretches the pulse in time.
ϕ_3	-	Changes the pulse shape, and stretches it in time.

the terms $\frac{\partial k}{\partial \omega}$ can be given by the following Taylor expansion of k around $(\omega - \omega_0)$,[28]

$$Lk(\omega-\omega_0) = \underbrace{k_0}_{\phi_0 \text{ - Carrier Envelope Phase}} + \overbrace{\frac{\partial k}{\partial \omega}}^{\phi_1 \text{ - Group Delay } (v_g^{-1})}(\omega-\omega_0) + \frac{1}{2}\underbrace{\frac{\partial^2 k}{\partial \omega^2}}_{\phi_2 \text{ - Group Velocity Dispersion (GVD)}}(\omega-\omega_0)^2 + \frac{1}{6}\overbrace{\frac{\partial^3 k}{\partial \omega^3}}^{\phi_3 \text{ - Third Order Dispersion (TOD)}}(\omega-\omega_0)^3 + ... \tag{17}$$

the terms for $\Phi(\omega - \omega_0)$ are more simply written as

$$\Phi(\omega-\omega_0) = \underbrace{\phi_0}_{\text{Carrier Envelope Phase}} + \overbrace{\phi_1}^{\text{Group Delay } (v_g^{-1})}(\omega-\omega_0) + \frac{1}{2}\underbrace{\phi_2}_{\text{Group Velocity Dispersion (GVD)}}(\omega-\omega_0) + \frac{1}{6}\overbrace{\phi_3}^{\text{Third Order Dispersion (TOD)}}(\omega-\omega_0). \tag{18}$$

The variables ϕ_n describe how the waveform of a pulse is altered after being dispersed by a medium. Each of the ϕ_n components contribute differently to the resultant dispersion, exactly what is most evident after the pulse is transformed back to the time domain. Table 1 lists the effects that each ϕ_n applied in the dispersion of the frequency domain has on the time domain. And while it is impossible to observe these effects acting on their own experimentally, Figure 3 shows exactly how each component affects a pulse.

These terms are important to include when attempting to estimate the photoinduced charge, since experimental setups will utilise a glass wedge system to control the phase by dispersion. Note specifically how the pulse amplitude in panels (d) and (e) are reduced as a result of ϕ_2 and ϕ_3, compared to the other factors ϕ that do not distort the pulse shape. This is because the resultant area under each must still equal the original pulse's.

E_t can be converted to E_ω using the Fourier transform, and the inverse Fourier transform for the reverse. However, since Figure 3 shows that the area under the pulse is preserved, the amplitude $\sqrt{I_t}$ from Equation 12 can be applied only after having calculated dispersion. This changes the electric field pulse into a vector potential pulse $a(t)$ instead, which can be then be converted into the frequency domain, have the dispersion factor $e^{-i\Phi(\omega-\omega_0)}$ applied, and transformed back before applying the electric field amplitude. This still generates the temporal effect of dispersion expected for an electric field.

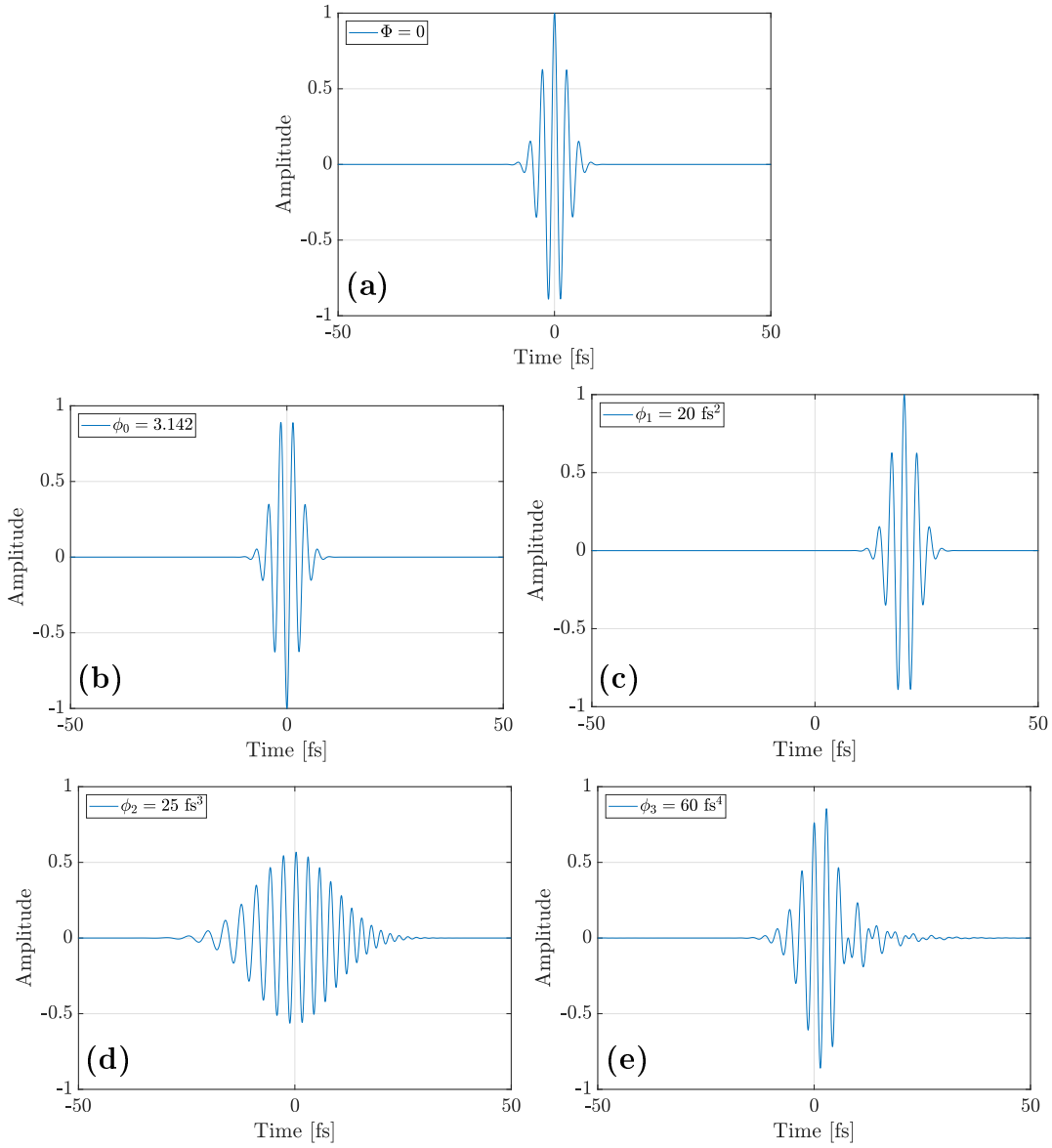

Figure 3: Graphs showing dispersion limited to one ϕ_n each. Panel (a) shows $\Phi(\omega - \omega_0) = 0$, and panels (b) to (e) ϕ_0 to ϕ_3 respectively, demonstrating the effects detailed in Table 1.

2.3.3 Calculating Photoinduced Charge from Optical Bloch Equations

Khurgin's study [1] is solely based on nonlinear effects and utilises optical Bloch equations (OBE) to derive expressions of the current, and consequently charge, induced by the incident laser radiation. With this approach, only the field asymmetry expressed as the potential vector momenta, the well-defined properties of the laser and the dimensions of the device itself are required. This method therefore completely circumvents atomistically resolved simulations, and the need for advanced band structure calculations per material. It forms these OBEs by expressing the Hamiltonian using the momentum gauge for the valence and conduction band energies and Kane matrix elements, and then solving the

differential equations generated when substituting the Hamiltonian into the evolution of density matrix. Solving the differential equations gives the following OBEs:[1]

$$\begin{aligned}\dot{x} =&(\omega_{cv} - \delta\bar{\Omega})y - \frac{x}{T_2} \\ \dot{y} =&-(\omega_c v - \delta\bar{\Omega})x + z\bar{\Omega}_{cv} - \frac{y}{T_2} \\ \dot{z} =&-2\bar{\Omega}_{cv}y + \frac{(1-z)}{T_1}\end{aligned} \tag{19}$$

Where x, y, z are the Bloch vector components of the x,y and z axes, Ω_{ii} are the intra and interband Rabi frequencies for $i = c \wedge v$. T_1 describes the relaxation of the population, driving the vector towards the ground state at -z, and T_2 describes the dephasing of the coherence between the valence and conduction band states, $\delta\Omega$, meaning that it reduces the x- and y- components, which are the coherent superpositions of the two states. An adiabatic solution for these OBEs is outlined in Khurgin's paper,[1] and finds that the generated population of carriers are not equal between electron-hole pairs that have a different sign for their k-vector. It also confirms that the interference of even and odd transitions are the only ones that generate a nonzero current, effectively allowing for any even numbered photon excitation pathways to be disregarded in further calculations.

With knowledge of the transitions that occur, it is possible to take the sum of the carrier densities in both bands over the whole Brillouin zone, effectively allowing for the current to be calculated. Khurgin eventually justifies that the vector potential $\bar{a}(t)$ of the laser pulse, along with the field strength F_0 and the nonlinear optical conductivities $\sigma^{(n)}$ can be used to define the current[1]

$$\bar{J}(t) = \sigma^{(3)} : \bar{a}(t)\bar{a}(t)\bar{a}(t)F_0^3 + \sigma^{(5)} : \bar{a}(t)\bar{a}(t)\bar{a}(t)\bar{a}(t)\bar{a}(t)F_0^5 + ... \tag{20}$$

for the terms that describe the interference of 1 vs 2 photons (3 in total) and 2 vs 3 photons (5 in total) and so on. Since it can be assumed that each pulse is well defined, and infinitely separated from the next, integrating this equation over the length of a single laser pulse gives the photoinduced charge[1]

$$Q_{2D} = \sigma^{(3)}\omega_0^{-1}F_0^3\left\langle a^3\right\rangle + \sigma^{(5)}\omega_0^{-1}F_0^5\left\langle a^5\right\rangle + ..., \tag{21}$$

which can be further simplified by reducing the nonlinear susceptibilities to[1]

$$\sigma^{(n)} \approx \varepsilon_0 F_0 \left(\frac{F_0}{F_a}\right)^{n-1} \tag{22}$$

where the atomic field F_a, a material constant, was determined to be approximately 5.36×10^{10} Vm^{-1} in fused silica, and was obtained by matching experimental results [9] to this model, making it a semi-empirical model. As a result, since the total photoinduced charge in the device should equal $Q = A_{eff}Q_{2D}$, where A_{eff} is the effective area of the device that could be illuminated, the final charge can be given as [1]

$$\begin{aligned} Q =& \left[\varepsilon_0 F_0 \left(\frac{F_0}{F_a}\right)^2 \left\langle a^3 \right\rangle + \left\langle a^5 \right\rangle \varepsilon_0 F_0 \left(\frac{F_0}{F_a}\right)^4 + \left\langle a^7 \right\rangle \varepsilon_0 F_0 \left(\frac{F_0}{F_a}\right)^6 + ...\right] A_{eff} \\ =& \varepsilon_0 F_0 \left(\frac{F_0}{F_a}\right)^2 \left[\left\langle a^3 \right\rangle + \left\langle a^5 \right\rangle \left(\frac{F_0}{F_a}\right)^2 + \left\langle a^7 \right\rangle \left(\frac{F_0}{F_a}\right)^4 + ...\right] A_{eff}. \end{aligned} \tag{23}$$

Here, ε_0 is the permittivity of free space, F_0 is the optical field strength (usually on the order of 10^{10} Vm^{-1}).

Finally, the vector potential momenta $\langle a^{2n+1} \rangle$ are the time integrals of the vector potential $a(t)$. It is arguably the most important factor in determining the strength of the optical-field-induced currents, mainly because it shows the characteristic measure of asymmetry that generates the driving electric field pulse. Since only odd powers of this potential will have non-zero integrals, the vector potential momenta can be found as

$$\left\langle a^{2n+1} \right\rangle = \omega_0 \int_{-\infty}^{\infty} (a(t))^{2n+1} dt, \tag{24}$$

as given in Khurgin's model. [1]

While this model was designed specifically for determining the photoinduced charge resulting from a the field asymmetry of a single ultrashort pulse, it could potentially be used for two-colour systems. The field asymmetry can be created by aligning two beams of coherent laser radiation, both with the same polarisation, so their waveforms are superimposed. If the pulse incidence is modulated in time, then varying degrees of field asymmetry can be gauged. Equations (24) and (23) can thus also be used to estimate the photoinduced charge for this case. The vector potential $a(t)$ simply becomes the sum $a(t) = a_{\omega_1}(t) + a_{\omega_2}(t)$ of the two incident lasers, after which its vector potential momenta and induced charge can be calculated in the same way as for a single pulse.

2.3.4 Photoinduced Charge from Cross Polarised Beams

Khurgin also evaluates the study by Schiffrin et al, [9,20] attempting to produce a model that confirms some assumptions about the nature of pump probe photoinjection, outlined in the studies by Schiffrin [9] and Paasch-Colberg [10] et al, where the weak electric field

of a visible/near infrared light pulse was measured. In the experiment, two orthogonally polarised pulses are combined on the surface of a SiO_2 sample, and the photoinduced charge measured as one of them is delayed by Δt. The pump component, known as the injection pulse, has a strong field amplitude and is polarised in the y direction (perpendicular to the intended current flow over the junction). The other pulse, known as the driving pulse, has a weaker field amplitude and is polarised in the x direction (contact to contact). When the delay of the injection pulse is altered by Δt, the photoinduced current is defined by the cross correlation moments, as can be seen in Equation (25).

$$Q(\Delta t) = \varepsilon_0 F_0 \left(\frac{F_{0y}}{F_a}\right)^2 \left[\frac{1}{3}\left\langle a^{2+1}(\Delta t)\right\rangle + \frac{1}{5}\left\langle a^{4+1}(\Delta t)\right\rangle \left(\frac{F_{0y}}{F_a}\right)^2 + \frac{1}{7}\left\langle a^{6+1}(\Delta t)\right\rangle \left(\frac{F_{0y}}{F_a}\right)^4 + ...\right] A_{eff} \tag{25}$$

Where the vector potential momenta are instead given by

$$\left\langle a^{2n+1}\right\rangle (\Delta t) = \omega_0 \int_{-\infty}^{\infty} \underbrace{a(t)}_{\text{Driving pulse } (F_{0x})} \overbrace{(a(t-\Delta t))^{2n}}^{\text{Injection pulse } (F_{0y})} dt. \tag{26}$$

The distinct difference here is that the contribution to the vector potential momenta is split between the weaker driving pulse, and the stronger injection pulse, where the shape is predominantly determined by asymmetry of the injection pulse.

3 Method

3.1 Device Fabrication and Design

Several devices of different architectures, substrates and contact materials were fabricated during the course of the project. While the main focus of this study was on the material properties of GaN that allows optical-field-induced currents to be generated,[10] SiO_2 and SiC samples were also fabricated to further investigate the phenomenon. Several iterations of different device architectures were trialled before settling on a final design. Figure 4 shows three separate device designs that were fabricated and used in experiments. While Design A was used as the initial design for the first devices, issues during both fabrication and experiments made it unsuitable for use. The $2-6$ µm junction has two narrow gold bridges defining the device region, but these small features are not only prone to overetching, giving a poor device yield, but also requires precise horizontal and vertical

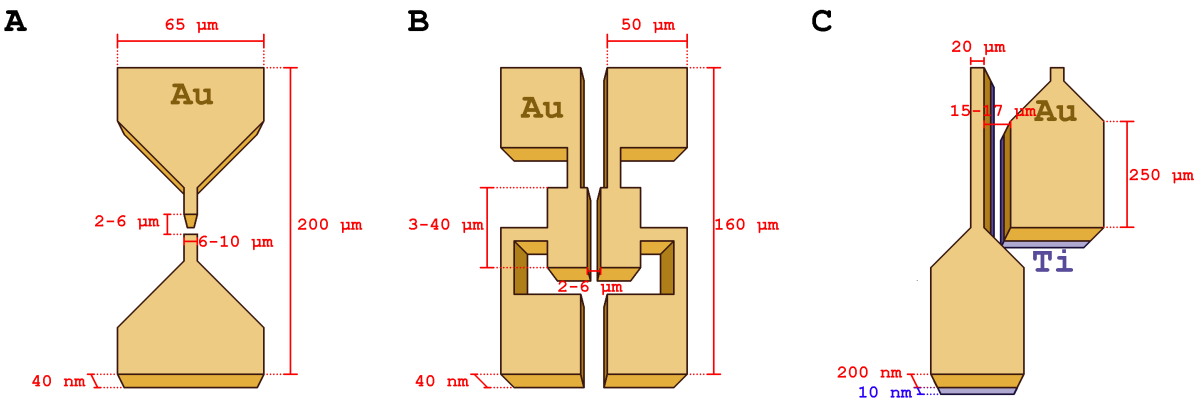

Figure 4: A graphic three separate device designs used in experiments. Designs A and B are intended to be fabricated using etching, while Design C would require the lift-off method.

laser alignment. As such, Design B was developed to have larger feature sizes, giving a higher device yield and, with a larger device area, requires only precise horizontal laser alignment.

Design C was originally intended to bridge nanowires across a wide 50 µm gap, but the adjacent contacts that lead to this gap are only separated by about 5 μm, which is well within the separation where the optical-field-induced currents should still be inducible.[9] The titanium adhesion layer provides better conductivity between the contacts and the substrate, something the other device designs lack.

3.1.1 Substrate Wafer Cleaning

Substrate samples are acquired by using a diamond scrape to cut a large disc of the desired material into smaller pieces (usually 8x4 mm or 4x4 mm), each of which is usually referred to as a die. This process results in large quantities of fine particulates being created, and therefore cannot be done within a cleanroom. Consequently, the surface of the wafer will be contaminated with dust and oils from previous handling when being brought into the cleanroom lab, and as such must be cleaned before it can be used in device fabrication.

The cleaning process is a standardised procedure that is carried out for all new samples, and is relatively straightforward: the sample is treated in three separate sonicator solvent baths, lasting a minute each. The first solvent bath is acetone, which removes the majority of oils and other soluble materials present on the surface of the wafer. The last two solvent baths are both isopropyl alcohol (IPA), which removes leftover acetone and other residues. Between each solvent bath, the sample is rinsed in a separate beaker of IPA before finally

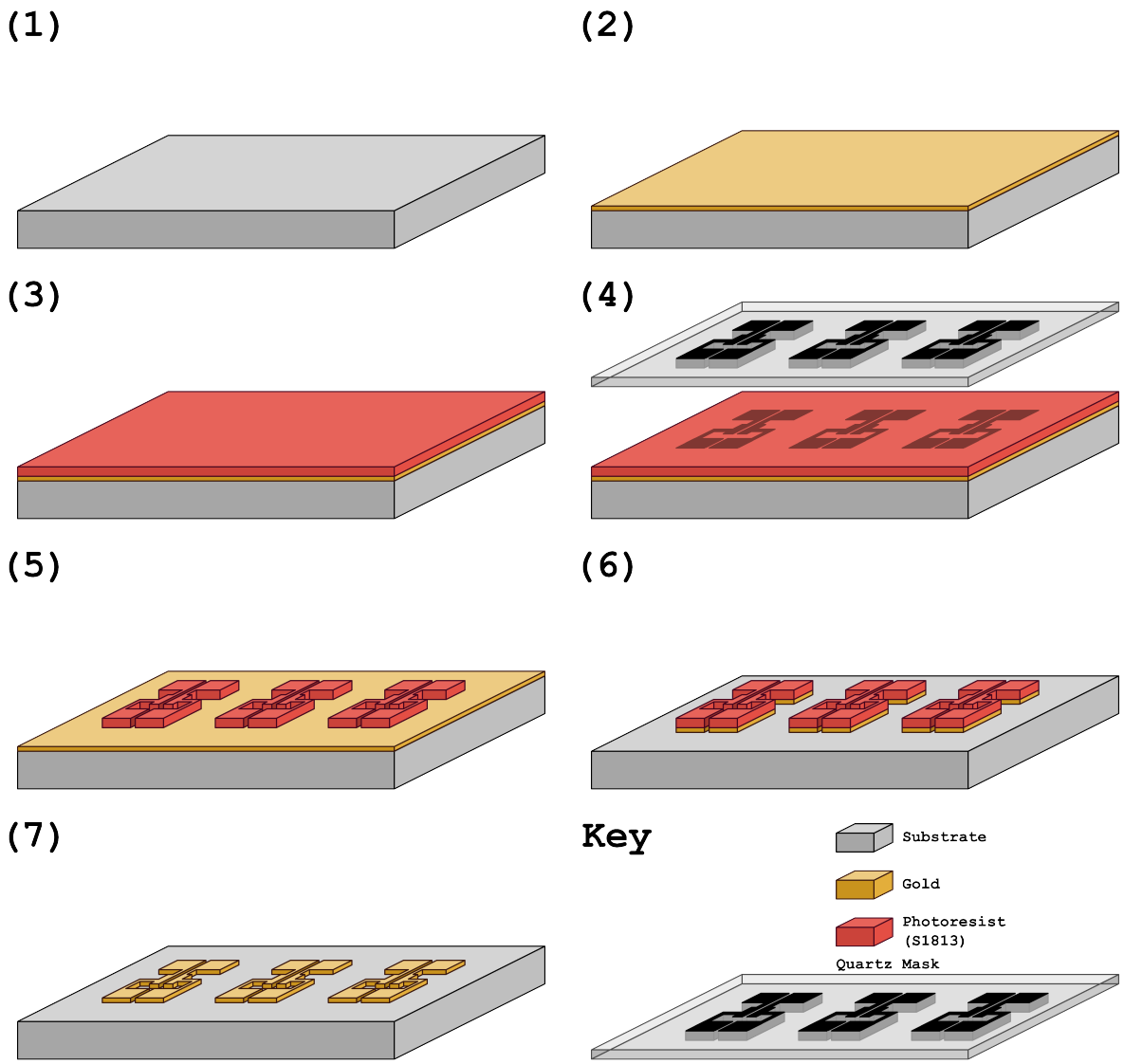

Figure 5: A visualisation of the appearance of the substrate wafer in the different steps of the recipe used to fabricate devices using gold etching. The panels show: (1) Cleaned substrate wafer. (2) Gold deposition (30-40 nm). (3) Photoresist deposition (S1813) and baking. (4) Mask transfer by hard contact soft UV lithography. (5) Photoresist development in MF-319. (6) Gold etching (7) Residue removal and sample cleaning

being dried using N_2.

3.1.2 Device Fabrication by Etching

Etching is a method whereby an acid, called an etchant, is used to remove a specific region of deposited metal around a device mask placed on top. Figure 5 shows a visual aid of the steps involved in creating gold contacts on a substrate wafer. First, the substrate wafer is cut to a suitable size, after which it is cleaned. Then, 30-40 nm of gold is deposited onto

the substrate wafer using an evaporator tool, such as an AVAC, used in this study. The maximum thickness of gold is determined by the rate at which the selected gold etchant removes the gold, where too thick a layer will undercut the mask sooner than removing all the gold down to the substrate. Following this, S1813, a positive photoresist, is spin coated onto the sample and is subsequently baked for for 90 s at 115 °C on a hotplate. Hard contact soft UV lithography is then used to transfer a suitable device pattern from a quartz photomask onto the sample using a mask aligner. If using a Mask aligner MJB4, as was in the fabrication of the devices for this study, then an exposure time of 5.5 seconds under standard settings is suitable. Since the exposed regions of the photoresist should now be soluble to the developer solution MF-319, the sample is then submerged in it for 50 s to dissolve all of the exposed photoresist. After rinsing in water to remove all residue, the developed mask should now be visible in an optical microscope. This is done to verify that the exposed photoresist was fully dissolved, so that the sample can be developed further if the pattern is not well defined. After a suitable mask has been developed, the sample is placed in gold etchant for 20 s, which should be long enough to remove all of the gold around the developed device pattern. Finally, after verifying that all gold around the mask has been etched away, all photoresist, and remaining etchant, is removed using acetone. The sample is then cleaning in IPA, followed by rinsing in water.

3.1.3 Device Fabrication by the Lift-off Method

Lift-off is a method whereby metal is deposited onto a device mask placed directly on the substrate, after which metal is deposited onto the sample, and the mask is "lifted off" to leave behind metal only where the substrate was uncovered by the mask pattern. Figure 6 shows a visual aid of the steps involved in creating titanium/gold contacts on a substrate wafer. A substrate wafer is cut to a suitable size, and is then cleaned. Before any photoresist is deposited, the wafer is prebaked for 300 s at 165 °C, and any remaining dust is blown off using N_2. LOR 10b is then spin coated onto the sample and baked for 300 s at 165 °C. Following this, S1813 is spin coated onto the sample, and is then baked for 90 s at 115 °C. Hard contact soft UV lithography is used to transfer a suitable device pattern from a quartz photomask onto the sample using a mask aligner. If using a Mask aligner MJB4, then 9 seconds of exposure time is suitable at 180 $mJcm^{-2}$. Compared to the mask when etching, this mask is inversed, exposing instead the device regions.

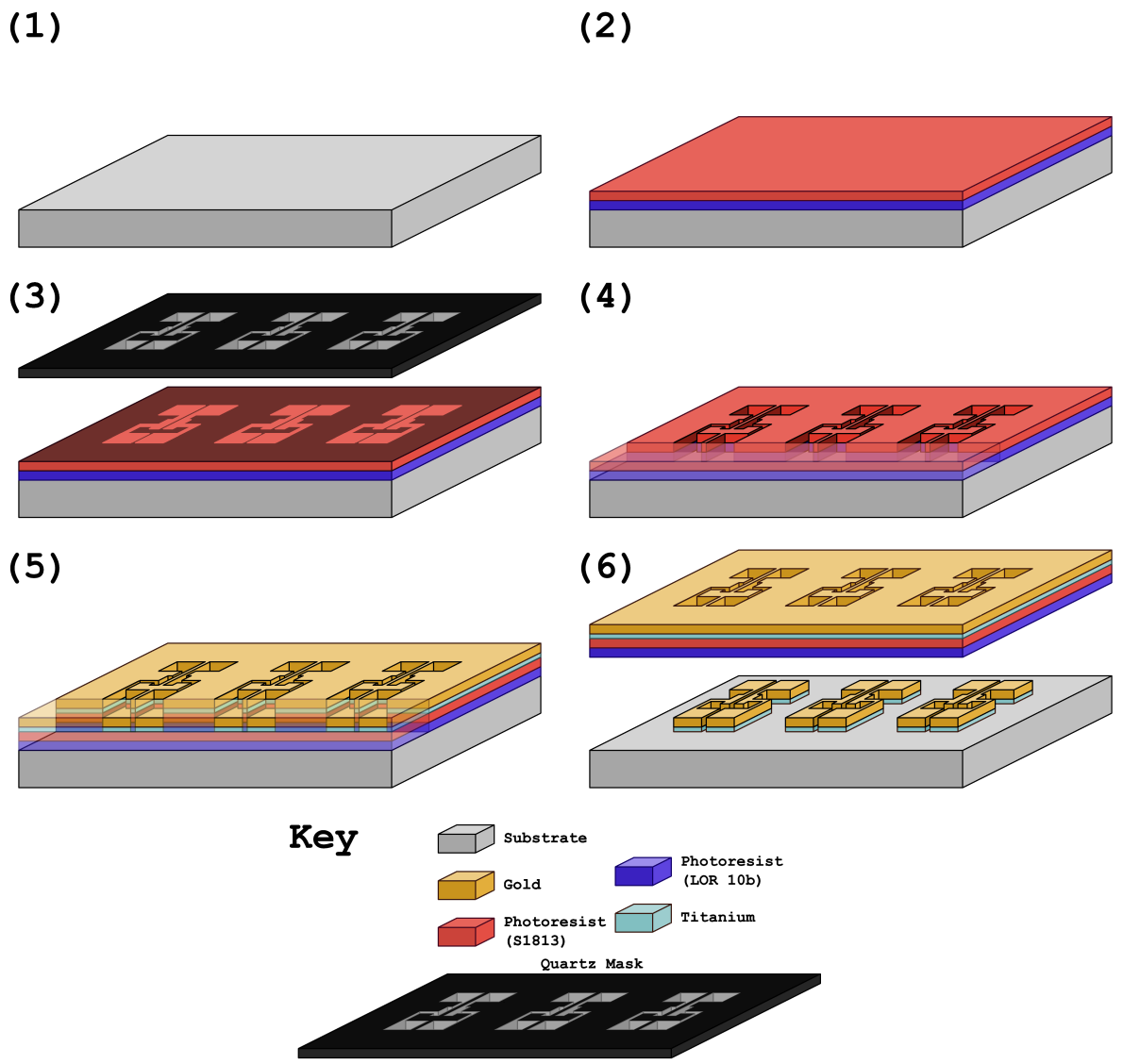

Figure 6: (1) Cleaned substrate wafer. (2) Photoresist deposition (LOR10b followed by S1813). (3) Mask transfer by hard contact soft UV lithography. (4) Photoresist development in MF-319. (5) Deposition of titanium (10 nm) followed by gold (200 nm) (6) Lift-off using Remover 1165

Consequently, when the sample is developed in MF319 for 50 seconds, the photoresist inside the areas that define where the metal contacts will be deposited is removed. After ensuring that the mask is well defined in an optical microscope, resist residues must be removed to ensure the metal is deposited directly onto the substrate. Thus, the sample is rinsed in water before being dried in N_2, after which a plasma-preener, run at 50 mbar for 30 seconds, can be used to remove the resist residues inside the device areas. Then, using an evaporator system like an AVAC, 10 nm of titanium, followed by 200 nm of gold, are deposited onto the sample. Finally, the lift-off is performed by placing the sample into a beaker of Remover 1165, heated to 90°C, for 40 minutes. This is immediately repeated

with a new beaker of Remover 1165 for another 15 minutes. To remove the remaining gold residue, the sample is cleaned with water, then with IPA and is then dried with N_2.

In the final developed resist pattern, the divide between the elevated regions still covered with resist, and the lowered regions without any, is called a step. The shape of this step will directly influence the ratio of thickness of evaporated material near the top, compared to the bottom of said step. This ratio is known as the step coverage, and it describes the thickness uniformity of the evaporated material down the step. Good step coverage implies a high level of uniformity, and poor step coverage sees a lower thickness near the bottom of the step. When performing a lift-off, the ideal conditions see a poor step coverage, since this allows the material deposited within the developed device regions to be more well defined, and separate more easily from the material on the resist during lift-off. This is why the combination of LOR 10b (a non UV sensitive resist), and S1813 (a UV sensitive photoresist) is used. When the sample is exposed, only certain regions of the S1813 become soluble in the developer, meaning that the LOR 10b will only develop after and underneath the S1813. If the time of development is too short, there is no undercut, if it is too long, then the overhang might collapse, which in turn gives a poor step coverage as desired.[29] Figure 7 shows an example of both good and poor step coverage. The poor step coverage illustrates why the development process must be allowed to create a

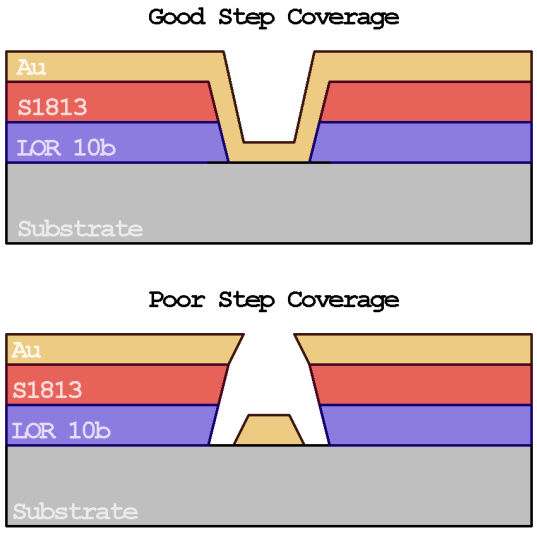

Figure 7: Two examples of resist development, one with a good step coverage, and the other with poor step coverage. Good step coverage will cause deposited materials to join up, risking their removal during lift-off.

resist undercut when fabricating a device by lift-off, since without it, the metal deposited directly onto the substrate is more likely to be removed along with the material deposited on the resist.

Devices fabricated using optical lithography and lift-off tend to have a low resolution, meaning the smallest feature size is relatively large, and wall surfaces have poor smoothness, ending up uneven and jagged. For many devices, this does not pose a problem, but plasmonic hotspots may become an issue if the material used for the contacts is not a refractory metal.

A solution to this would be the use of Electron Beam Lithography (EBL) instead. This procedure is near identical to the one described in Figure 6, except the resist exposure is done using an electron beam, and instead of using both LOR and S1813, only PMMA is used. This technique has a much higher resolution, smoother edges, and a higher success rate. The biggest disadvantage is the time it takes to complete one device. When making a new device design, a large amount of time is required to simply plot it out in a piece of software known as K-Layout, add to this the time it takes to operate the EBL system and the procedure is the most time consuming of the three.

3.2 Experimental Set-up

After fabrication, each finished sample is examined through an optical microscope to determine if there exist any candidate devices. These are characterised by well-defined contacts, and fully separated source and drain contacts. Up to seven identified devices are then wire bonded to a chip, and their functionality is verified by measuring their current-voltage characteristics (IV-curves). The setup used to measure the IV-curves of each device can be seen in Figure 8. The ideal device should have an IV curve that isn't fully linear, showing some increased resistance near zero volts.

After a long apparatus development, the circuit shown in Figure 9 was eventually finalised, allowing for the direct measurement of the optically induced current from a wire bonded to device. This setup can be modified, while still using the Femto preamp, to measure IV curves as the setup in Figure 8 does.

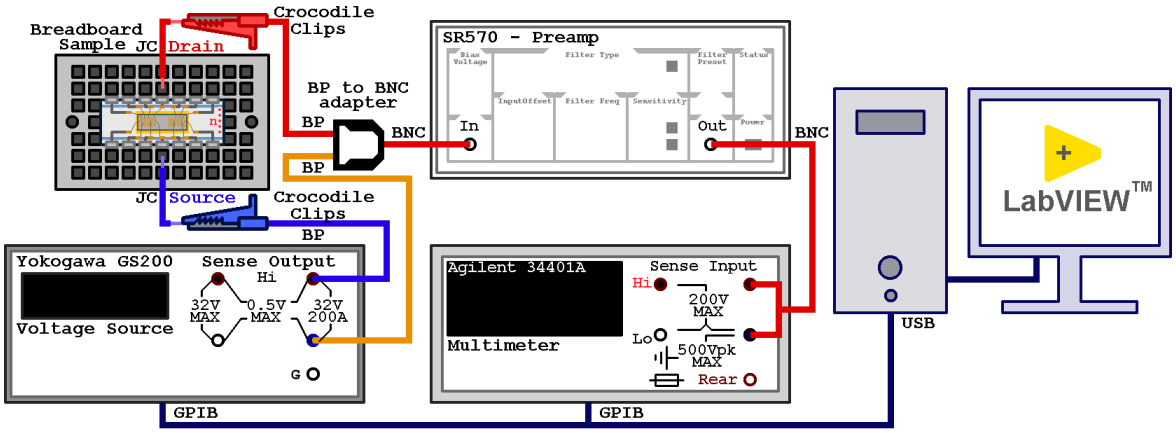

Figure 8: A device diagram showing the experimental setup used to measure IV curves of fabricated devices. The devices are connected by plugging jumper cables (JC) into the breadboard sockets that correspond to the source and drain of each device, then connecting these by attaching crocodile clips to the exposed wires, connecting the full external circuit. The voltage source and multimeter can both be controlled using a measurement software written in Labview.

3.3 Short Pulse Experiments - Titanium-Sapphire Laser

The laser source for these experiments is based on titanium-sapphire technology. The pulses from an actively phase-stabilized oscillator are amplified using optical parametric chirped pulse amplification. This technique is used in order to pertain the broad bandwidth during amplification, which is needed to support ultrashort pulse durations. This laser system has been described, for example, in a study by Harth et al.[30] It is capable of delivering 6-fs pulses with over 10 µJ of pulse energy. This is more than sufficient to provide the high field strengths require for driving field-induced currents in GaN. Before experiments, the pulse duration at the focus is confirmed using the dispersion-scan technique.[31] The size of the focal spot is measured with a beam profiling camera. Then, using the setup detailed in Figure 9, the laser can be aligned, using the camera feed as reference, to the junction of the connected device, and the output current can then be measured. At higher laser intensities, the brightness of the laser spot oversaturates the CCD in an area much larger than the size of the junction. Tuning down the laser will reduce the size of the oversaturated area on the CCD to more closely resemble the actual laser spot size, after which alignment to the junction is far easier. For devices with too small features to accurately judge the alignment from the camera alone, fine adjustments can be made to maximise the current reading on the lock-in. The highest achievable current should be considered the ideal alignment of the laser spot to the device junction. The current

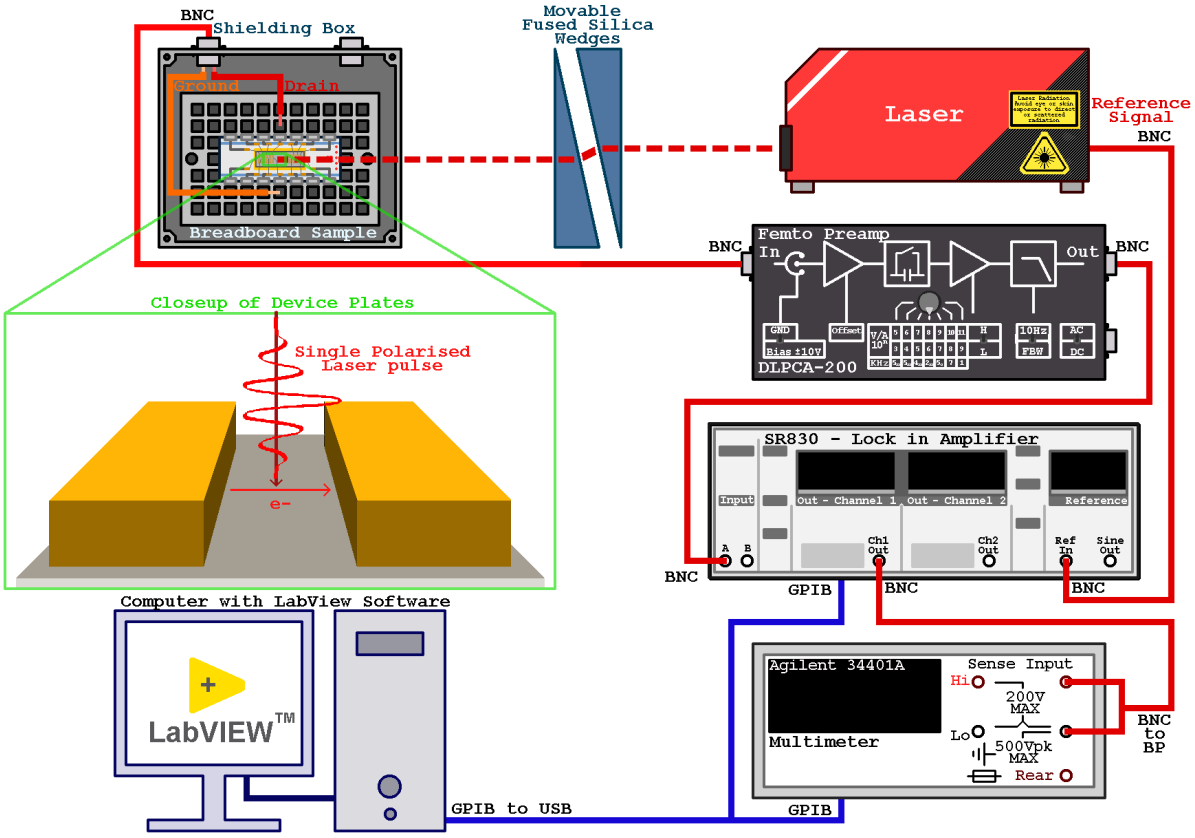

Figure 9: A graphic showing the final device setup used to measure optical-field-induced currents with the Ti:Sa laser. At this point, all unshielded cables have been replaced with shielded ones, that all have BNC connectors. The device samples are now in a shielding box, with internal and external BNC connectors. This box, in turn, is mounted on a stage attached to the laser table via a metal rod that is glued to the box on a plastic cap, fully insulating the sample from the stage. A CCD camera attached on a magnifying lens tube is also mounted to the laser table, and the camera feed used to align the laser.

can then be measured as a function of the laser power, which is altered by adjusting a polariser pair. In an ideal case, the measurement process should be automated, where the current for each intensity of the laser should be measured over several seconds, and the weighted average calculated for each. Unfortunately, due to time constraints, the results were only gathered manually for this study.

If modulating the phase of a few cycle laser, the resultant asymmetry of each pulse will be altered, effectively changing the optical field strength incident on the sample. Thus, since the current is dependent on the resultant asymmetry, which in turn is dependent on the phase, a measurement can be made.

3.4 Two-Colour Experiments - Ytterbium Laser

A similar setup as can be seen in Figure 9 was used for the experiments using the Yb laser. However, when the measurements were being made, the SR570 preamp was still being used, as well as cable and breadboard solution as illustrated in Figure 8, spare that the then called Source was connected to the ground of the same BP to BNC adapter.

The main purpose of the two-colour experiments is to generate the optical-field-induced currents by creating an asymmetry with a two-colour wave overlap. The two separate colours are the fundamental frequency of the Yb laser, and its second harmonic, generated using a nonlinear process. These two beams are then realigned, and focused on the gap between the two plates of a connected device. The second harmonic generation, realignment, and pulse delay are all done using an interferometer setup, detailed in Figure 10. Unlike the ultrashort pulses of the Ti:Sa laser, the Yb laser itself has about 30 optical cycles per pulse, and thus each beam cannot induce a current on its own, but combining the fundamental and second harmonic generates a field asymmetry large enough to do so. The relative difference in time of arrival Δt can be altered by moving the stage shown in the figure, and since this is the only way to alter the current, a program was written to automatically move the stage before measuring the current.

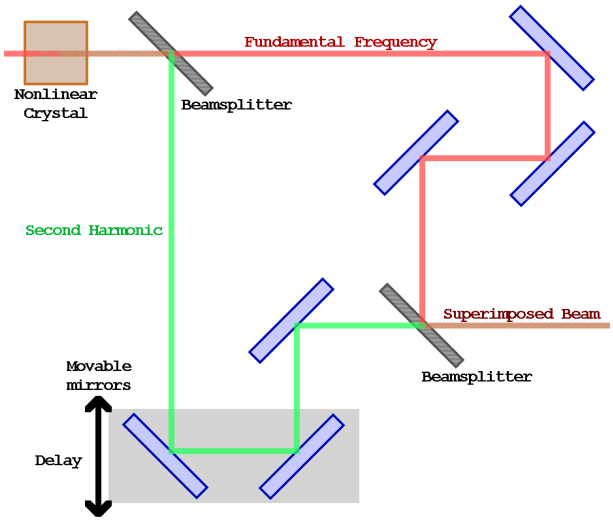

Figure 10: A diagram showing the general layout the Mach-Zehnder interferometer that was used to create and delay the second harmonic relative to the fundamental frequency in the Ytterbium laser setup

4 Results

This section will cover a range of results, including the variety of modelling implementations, the outcome of device fabrication, the development of the experimental setup, and finally the measurements from the attempts to observe optical-field-induced currents.

4.1 Modelling

The main purpose of reproducing Khurgin's model in MATLAB was to create a versatile tool that can be used to predict the outcome of experimental results. It was also expanded upon to include what was expected to be seen in the two-colour field experiments. As a consequence, a GUI was written specifically to handle the plotting of several different cases, while also allowing for the quick alteration of the relevant experimental variables. To further simplify this, a system was created that allows for specific settings to be saved as a preset that can be loaded to reproduce the same results at a later date. The full code, along with several presets used for for the plotting of the figures in this section, can be accessed in a GitHub repository.[32] In addition to the code, a more comprehensive readme file can be found, which further explains the use and implementation of the model. Appendix A also contains the script written to handle the Fourier transform, dispersion application, and inverse transform used in nearly every single result in this section.

4.1.1 Fourier-Transform-Limited Photoinduced Charge

If no dispersion is applied to the pulse, then the system is considered to be Fourier-transform-limited, meaning that it has the minimum duration for its spectral bandwidth. With this, the effects of the non-dispersive properties like the field strength and the number of optical cycles can be assessed. To determine the relationship between the number of optical cycles, and the asymmetry of the optical field, Equation (24) was used to calculate the vector potential momenta for several different optical cycles N_{cyc}. Figure 11a shows one plot of all $a(t)^{2n+1}$ when $N_{cyc} = 1.7$ for $n \in [0, 5]$. This shows how the peaks around the central maxima, whose amplitude remains constant, shrink with larger odd numbered terms, indicating an increasing asymmetry from higher power terms. This relationship is confirmed by Figure 11b, plotting instead the resultant asymmetry, expressed as the calculated integral $\langle a^{2n+1} \rangle$ under each equivalent $a^{2n+1}(t)$, for $N_{cyc} \in [1, 3.5]$. These two figures demonstrate not only that the resultant vector potential momenta increase with

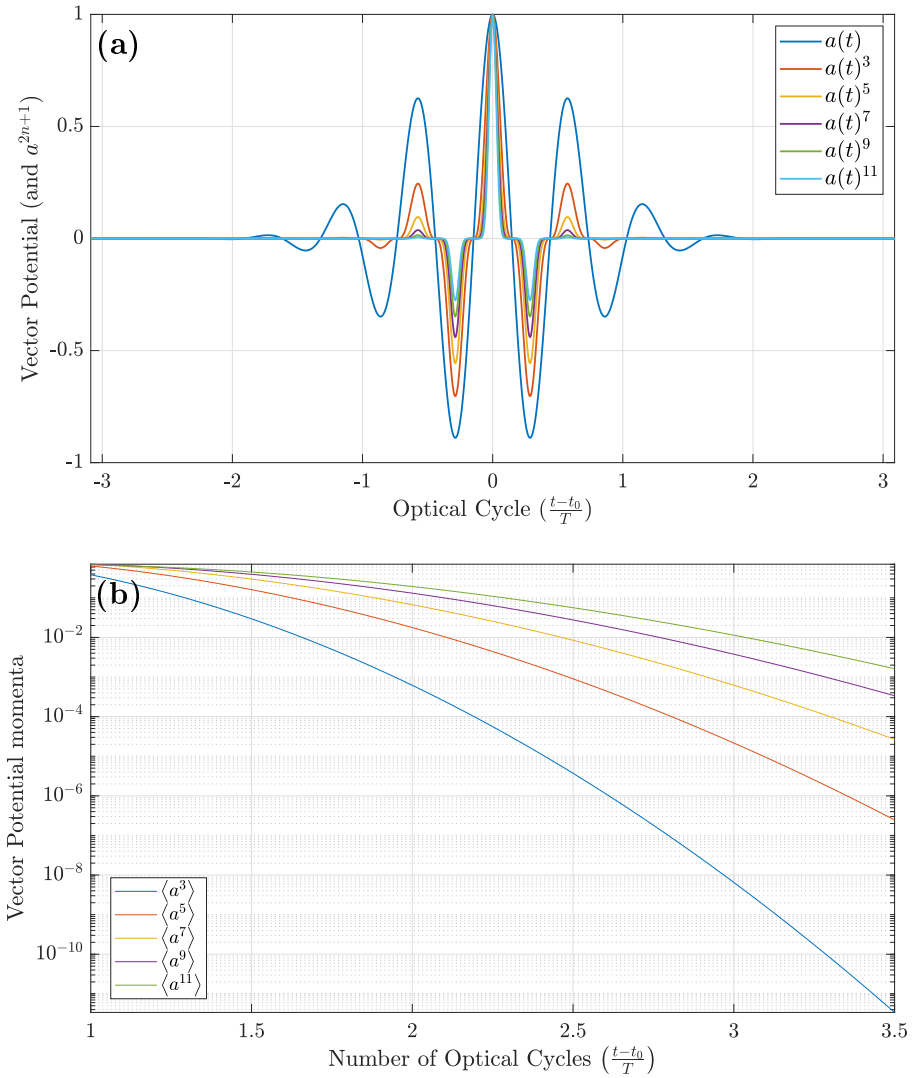

Figure 11: Here, panel (a) shows the real value plot of the odd powers of, and including, $a(t)$ from Equation (12) for a single pulse with $N_{cyc} = 1.7$, and $f_0 = 375$ THz. Panel (b) shows the vector potential momenta $\langle a^{2n+1} \rangle$ determined for each integral under $a^{2n+1}(t)$, one such pulse being shown in panel (a), calculated and plotted for values of $N_{cyc} \in [1, 3.5]$. These figures emphasise the importance of short pulses in generating larger photoinduced currents. An extended version of panel (b) can be found in Appendix A.

larger odd numbered terms, but also that increasing pulse length greatly decreases the resultant asymmetry of each term. However, the vector potential momentum is only one of the only contributing terms used when calculating the photoinduced charge.

If a non-dispersed laser pulse with field strengths $F_0 \in [0, 2.5] \times 10^{10}$ Vm^{-1}, matching the experimental explored parameter, is used to calculate the photoinduced charge using Equation 23, for $N_{cyc} = 1.7$, and the other variables used by Khurgin then Figure 12 is obtained. If, instead, the same estimate was made using any value $N_{cyc} > 3.5$, the pho-

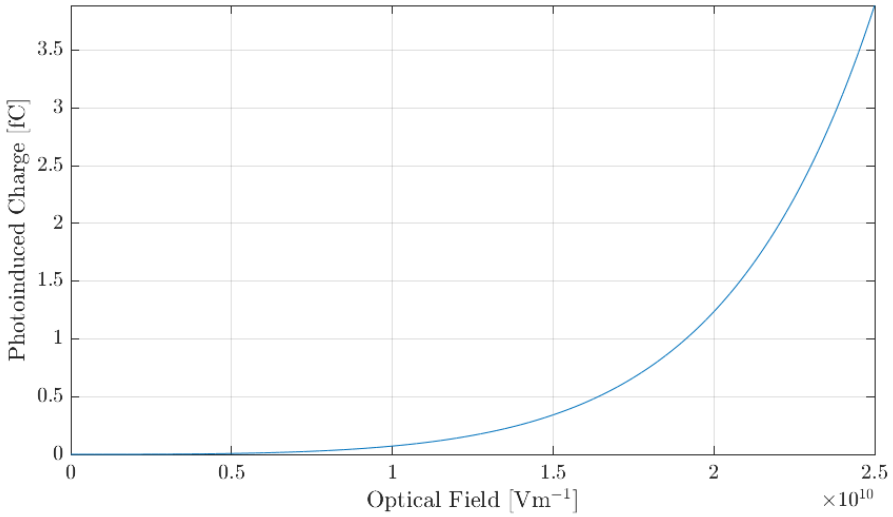

Figure 12: A graph showing the estimated photoinduced charge that the non dispersed pulse plotted in Figure 11a would induce at different field strengths $F_0 \in [0, 2.5 \times 10^{10}]$ Vm^{-1} on a device with $A_{eff} = 2.3 \times 10^{-12}$ m^2.

toinduced charge would be smaller than the elementary charge $e = 1.6 \times 10^{-19}$ C. This is further supported by Figure 27, which, as stated prior, shows that the asymmetry of $a(t)^3$ becomes negligible beyond $N_{cyc} > 4$. In the computer model, only terms up to $\langle a^{11} \rangle$ are considered, since the higher order terms only become significant within one order of magnitude after 3×10^{10} Vm^{-1}.

The magnitude of each term contribution is illustrated directly in Figure 13, where the term contribution to the photoinduced charge has been plotted to $\langle a^{101} \rangle$. The graph shows that the $\langle a^{13} \rangle$-term only becomes significant to one order of magnitude of the greatest contributing term at a fields strength of over 3.3×10^{10} Vm^{-1}. Since the model uses $F_a = 5.36 \times 10^{10}$ Vm^{-1}, Equation (23) shows that the $\left(\frac{F_0}{F_a}\right)^{2n+1}$ term should start to grow exponentially when F_0 becomes greater than F_a, which is why there is a slope change at exactly $F_0 = F_a$. Thus, if considering only the results from this model, it could be suggested that it should not be used to estimate results from field strengths of greater than 5×10^{10} Vm^{-1}, and needs to consider additional higher order terms beyond 3×10^{10} Vm^{-1}, noting specifically that the third order term only becomes smaller than the fifth order term at 1.7×10^{10} Vm^{-1}. However, experimental results suggest that it not straightforward, since the study by Schiffrin et al. found that, due to sample imperfections, the phenomenon breaks down at around 2.5×10^{10} Vm^{-1}.[9]

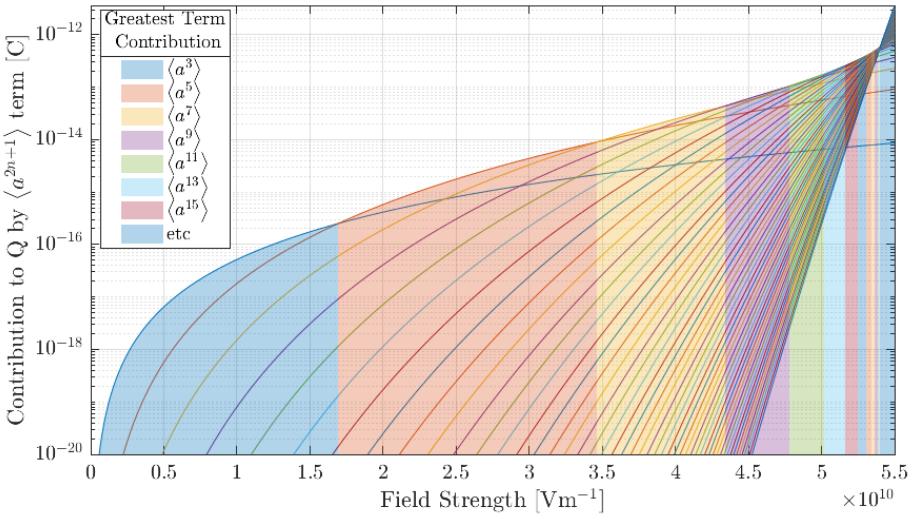

Figure 13: A plot of the photoinduced charge, given as the individual term contributions of all odd-numbered vector potential momenta up to $\langle a^{101} \rangle$ for $F_0 \in [0, 5.5] \times 10^{10}$ Vm^{-1}. The coloured area plots represent which term contributes most to the photoinduced charge for a given field strength. Note that at 5.35×10^{10}Vm^{-1}, the highest order term (any greater than $\langle a^{101} \rangle$) will always have the greatest contribution, since the $\left(\frac{F_0}{F_a}\right)^{2n+1}$ term becomes exponential when $F_0 > F_a$.

4.1.2 Photoinduced Charge of Chirped Laser Pulses

However, no experimental setup will have a truly Fourier-transform-limited system, since the laser pulse will always experience some dispersion before reaching the sample. This, however, can be used as an advantage to control the phase of incident pulses by altering the CEP. In the experimental setup for short laser pulses, the laser will be passed a propagation distance L through a pair of SiO_2 wedges, consequently introducing dispersion to the pulse. As a result of this, the model must also include a way to calculate the photoinduced charge induced by a dispersed pulse.

To do this, the dispersion factor for SiO_2 must be determined for a specific frequency. Online documentation was used to find an equation for the refractive index of SiO_2 in terms of the wavelength at $f_0 = 375$ THz.[33] Then, MATLAB was used to determine the first, second, and third derivatives which are used to define the terms of $\Phi(\omega - \omega_0)$.[27] These calculated dispersion factors are listed in Table 2, and are applied according to Equation (14) to Fourier-transformed time domain pulses before they are transformed back, now with applied dispersion. The dispersed pulses can have their vector potential calculated using Equation (24) and the photoinduced charge by Equation (23). Thus,

Table 2: A table containing the ϕ_n values resulting from the propagation of a laser pulse through SiO_2 when $f_0 = 375$ THz.[33] Since ϕ_0 describes a constant offset for all frequencies, it is set to zero as to mimic a phase locked laser. To get the dispersion factor, each term must be multiplied by the propagation length L

ϕ_0	=	0	mm^{-1}
ϕ_1/L	=	4.8478×10^{-12}	smm^{-1}
ϕ_2/L	=	3.6207×10^{-29}	s^2mm^{-1}
ϕ_3/L	=	2.7479×10^{-44}	s^3mm^{-1}

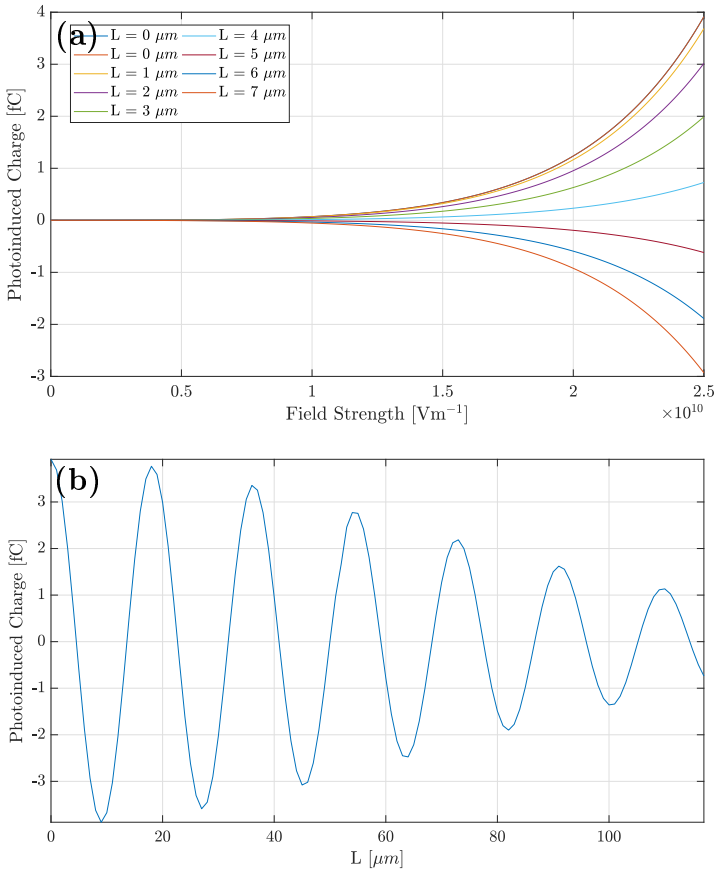

Figure 14: Panel (a) shows the generated photoinduced charge with a field strength of $F_0 = [0, 2.5] \times 10^{10}$ Vm^{-1} for propagation lengths $L \in [0, 7]$ µm. Panel (b) shows generated photoinduced charge at $F_0 = 2.5 \times 10^{10}$ Vm^{-1} for values $L \in [0, 120]$ µm. These graphs illustrate what should be observed experimentally when moving glass wedges in front of a laser, such as those in Figure 9.

Figures 14(a) and 14(b) were generated using the same variables as used in Figure 12, but with a varying dispersion propagation distance L, to illustrate what is expected to be observed when moving the wedges in the experiments. From the figure, there's a clear link between the propagation distance and the resultant charge, not only is there an os-

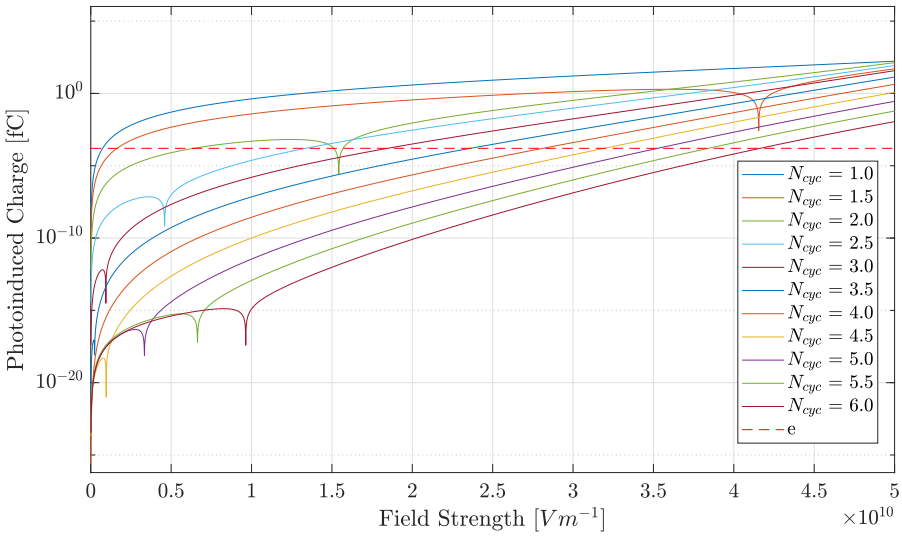

Figure 15: A graph showing the photoinduced charge calculated for pulses with increasing N_{cyc}. A dispersion length of $L = 0.1$ mm was used to apply dispersion to the pulses before calculating the photoinduced charge resulting from field strengths $F_0 \in [0, 5] \times 10^{10}$ Vm^{-1}. The elementary charge $e = 1.6 \times 10^{-19}$ C is also plotted to highlight that short pulses, or very high field intensities, are required before a current is expected to be seen.

cillation with a sign inversion, but there is a gradual decrease of the maximum charge as L increases.

To further show that short pulses are required to generate a charge, Figure 15 was generated for increasing N_{cyc} for a larger range F_0. Note that, the dips in each curve are caused by an issue with both under-sampling, and choosing a too small a time axis around the plotted pulses when determining the values for $\langle a^{2n+1} \rangle$. The first few orders of $a(t)^{2n+1}$ do not quite reach zero at the limits of the time axis, and thus contribute a minimal negative resultant vector potential momenta, that is eventually overcome by the next positive term. For these, 1,000,000 sampling points were taken in $t = [-700, 700]$ fs, even when the pulse duration was only 160 fs, when creating and evaluating each integral. The increase in field strength should not change the sign of the generated photoinduced charge, so the dips should be disregarded.

In spite of the issues with under-sampling, these results further solidify that experiments using the Ti:Sa laser, which has pulses with a number of optical cycles $N_{cyc} \approx 2.5$, should require only a field strength of about 1.3×10^{10} Vm^{-1} before a current measurement should be possible to measure.

4.1.3 Two-Colour Photoinduced Charge

In order to model the expected results from a two-colour experiment, the model of Khurgin is invoked with a modified driving field. The symmetry breaking that can be achieved by mixing only a few percent of second harmonic to the fundamental waveform is significant, as shown in Figure 16. The figure was created by calculating the photoinduced charge from the vector potential produced by the per-element addition of the first and second harmonic pulse vectors. The relative delay in each case was generated by circularly shifting the matrix elements of one of the pulses using `circshift(A,n)`, where A is the pulse matrix and n the units by which it is shifted. The delay Δt is therefore given by $n \times dt$, where dt is the smallest time axis interval of the generated pulses. Each pulse effectively have a near-zero resultant vector potential momenta, but when the positive centre peaks of the two pulses are aligned, their peak offset means that every trough on the fundamental is destructively interfered with by the second harmonic whereas every peak is constructively interfered with, something that is clearly visible in Figure 16a.

Unlike the ultrashort pulse case, the magnitude of photoinduced charge produced by the

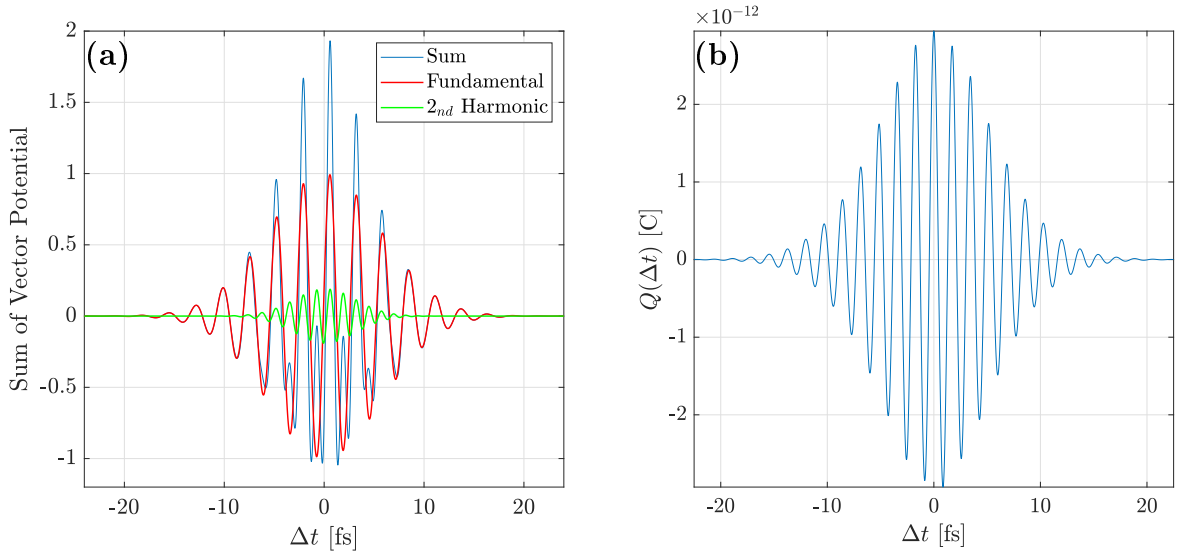

Figure 16: Using the central frequency $f_0 = 291$ THz and a number of optical cycles $N_{cyc} = 3.5$, the first and second harmonic vector potential are superimposed, and their sum taken, at varying temporal delays of $\Delta t \in [-25, 25]$ fs. Panel (a) shows one such superposition at $\Delta t = 0$, where the intensity of the second harmonic has been reduced to demonstrate where the constructive interference occurs. For each Δt, the resultant vector potential is taken, and the optical-field-induced charge calculated, which is shown in panel (b). For these results, the field strength of the fundamental was set to $F_0 = 2.5 \times 10^{10}$ Vm^{-1}, and the second harmonic $F_0 = 1.5 \times 10^{10}$ Vm^{-1}

two-colour superposition is on the order of 10^3 fC, a thousand times greater than with the single ultrashort pulse. Because of this, it's justified that less sensitive equipment can be used to measure current from any samples durable enough to be placed under the laser.

4.1.4 Photoinduced Charge from Cross Polarised Beams

Finally, since Khurgin also covered orthogonally polarised beams in a driving-injection pulse system, its implementation was replicated for the sake of potential future studies on the topic. As with the two-colour model, `circshift(A,n)` is used to delay one of the pulses relative to the other. This time, however, the vector potential momenta are calculated using Equation (26), and the photoinduced charge by Equation (25), where the results can be seen in Figure 17.

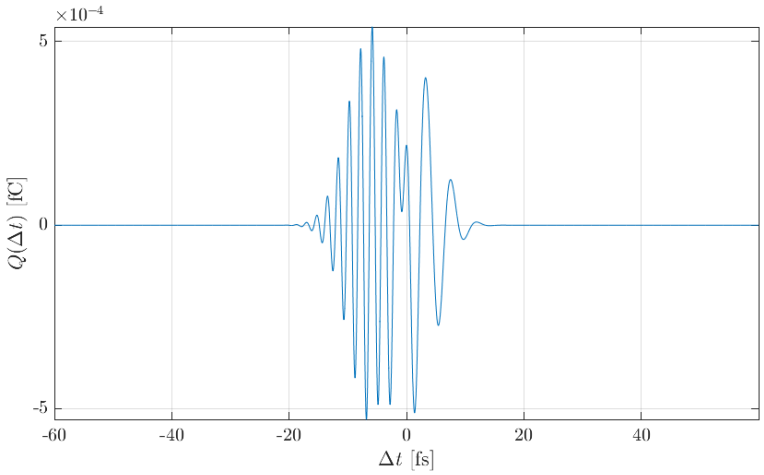

Figure 17: Cross polarised photoinduced charge of two pulses with $f_0 = 375$ GHz, plotted using the following parameters. $L = 0.1$ mm, $F_{0x} = 2.5 \times 10^{10}$ Vm^{-1}, $F_{0y} = 5 \times 10^{10}$ Vm^{-1}, $N_{cycx} = 1.6$, $N_{cycy} = 3.5$. While not identical to the results by Khurgin et al (Fig. 5. c),[1] it shares many features like the centralised peak large trough followed by a high peak, and a trailing section beyond that increases to the rightmost smaller peak in two steps.

With a pump probe photoinjection setup, these results could too be replicated and compared to experimental data, just as in the study by Khurgin, where the experimental data from the study by Schiffrin et al was used as a basis for the model.[9] [1]

4.2 Sample Devices

During the course of this study, much time was spent on fabricating new sample devices that could be used in experiments. Thus, a wide variety of device designs, substrate

materials and fabrication procedures were tested and iterated upon in attempts to produce devices with well defined, and smooth edged contacts.

4.2.1 Device Turnout

A total of 15 samples, containing up to seven devices each, were successfully fabricated, and from these, 40 devices were wire bonded to a chip, and were ready to be used in experiments. Nearly all devices were fabricated using gold etching, on mostly GaN-Sapphire substrates, but SiC and SiO_2 substrates were also used. Figure 18 shows three wire bonded devices, and a candidate device from four separate samples.

The two steps that ruined the most amount of devices was the UV mask development, and even if succeeding that, the etching that followed. The biggest pitfall in the mask development comes from the verification step after leaving it in the developer, since this

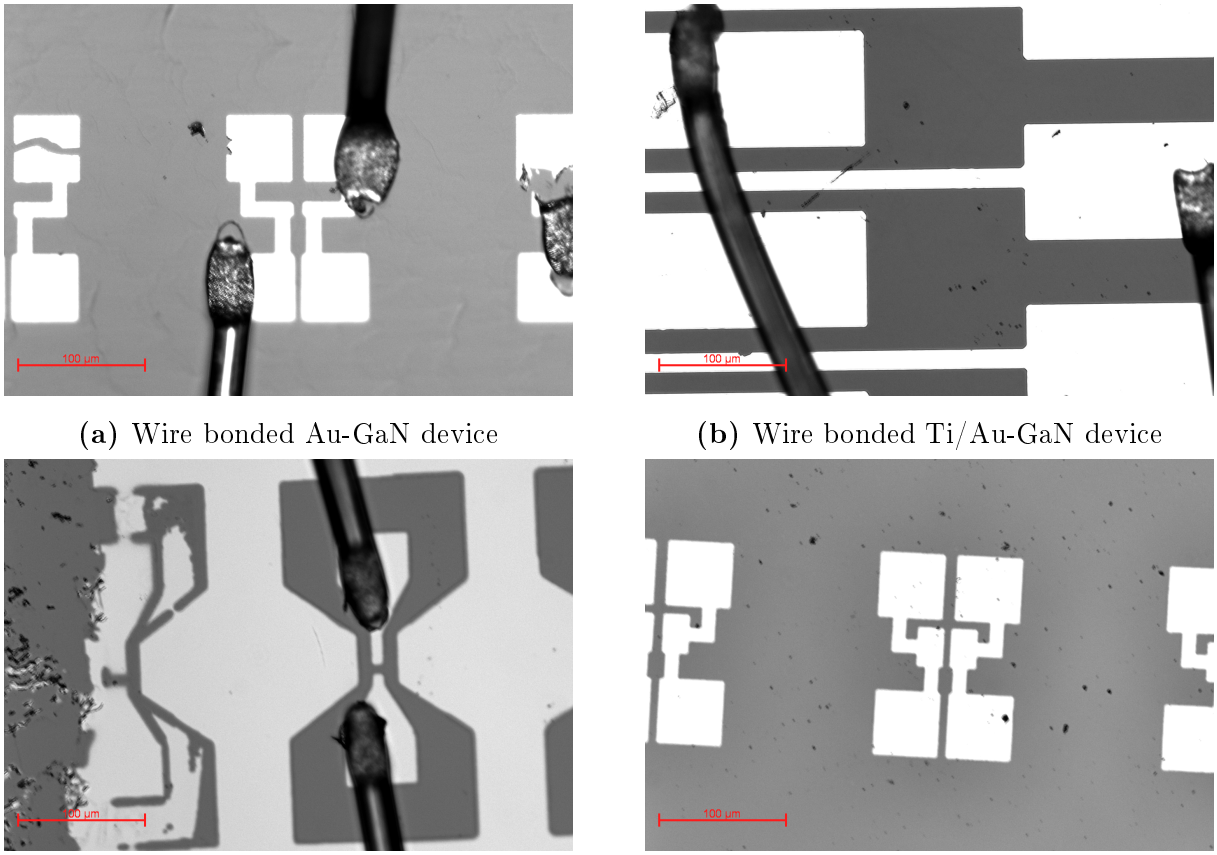

(a) Wire bonded Au-GaN device

(b) Wire bonded Ti/Au-GaN device

(c) Wire bonded Au-GaN device

(d) Unbonded Au-SiC device

Figure 18: Images taken of several fabricated devices. With reference to the device designs from Figure 4, panels (a) and (d) show device design B, (b) device design C and (c) device design A. Note how the device in panel (c) shows minor signs of overetching, since the bridges should not have rounded edges.

process sometimes requires more time than recipe calls for. Discerning whether or not there is a thin film residue in the device pattern is difficult, since the resist is transparent, and especially so when only a thin layer remains. Several samples were thought to have fully developed masks, but during etching it was revealed that thin film residue remained, leaving most devices partially etched, and with no conceivable way to salvage them. Consequently, even when the mask is well defined, overetching and underetching are both equally challenging to avoid. Figure 19 shows four separate samples with a variety of device fabrication defects.

From the figure, panel (a) shows a severely overetched device caused by a failure to identify a completed etch in the optical microscope, and then increasing the etch time. Even with a well defined mask, as is indicated by the well defined mask outline around the overetched regions, the etching step has very strict timings for well defined devices.

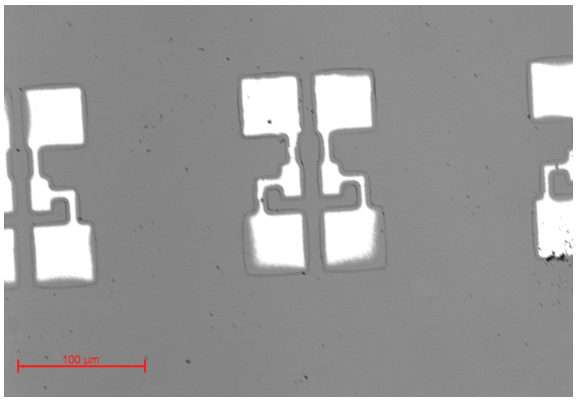

(a) Overetched Au-SiO_2 device

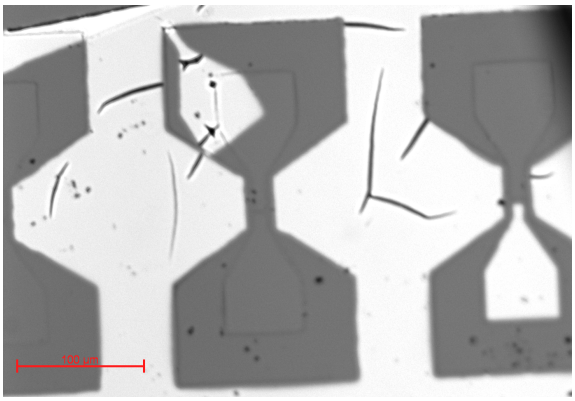

(b) Adhesion failure on Au-GaN device

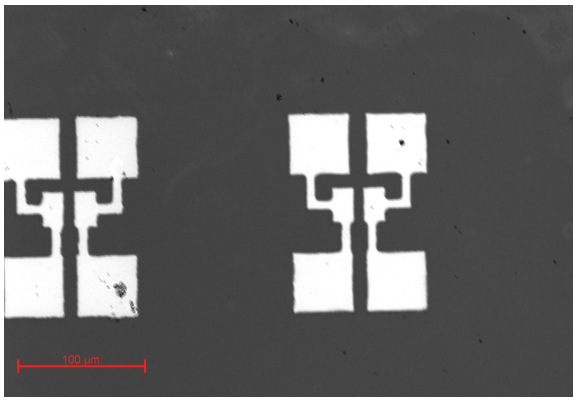

(c) Minimal overetching on Au-GaN device

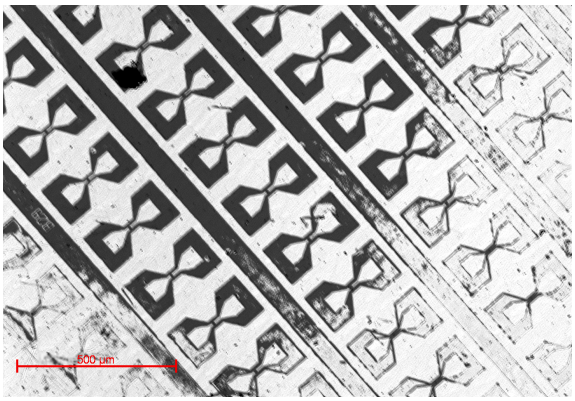

(d) Underetching on Au-GaN device

Figure 19: Images of faulty devices. Panel (a) shows a device that was overetched after a making a well developed mask. Panel (b) shows the adhesion failure of gold contacts that were otherwise etched properly. Panel (c) shows a candidate device with minor overetching, featuring rough edge details. Finally, panel (d) shows underetching caused by a poorly defined mask.

The device in panel (b) supports the requirement of an adhesion layer, because while the contacts themselves are well defined, the gold failed to adhere to the GaN, being swept away during etching. The device in panel (c) is an example of acceptable etching damage, having well enough defined contacts to be a candidate device, but has some rough edge definition, meaning it would be susceptible to the generation of plasmonic hotspots. Finally, the devices in panel (d) were created by a failure to identify a fully developed mask, since a few regions did not fully have the resist developed and removed, causing underetching to be the prevailing issue.

An ideal device should not have linear IV-characteristics. Table 3 contains the estimated resistances of devices whose IV-curves were measured, and Figure 20 shows the IV curves from four Ti/Au-GaN devices on D10. The resistances were calculated by determining the gradient inverse of a polynomial fit generated near zero bias voltage, usu-

Table 3: A table containing the estimated near zero resistance of 20 different device IV-Curves. Effectively, this is the sum of the metal to substrate, and substrate sheet, resistances.

Materials	Device	Resistance [Ω]	Material	Device	Resistance [Ω]
Au-GaN	D7b1b2	6.1525	Ti/Au-GaN	D10t7b7	26.1061
Au-GaN	D7b3b4	85.9652	Au-GaN	D11b1b1	37.5854
Au-GaN	D7t2t3	58.5395	Au-GaN	D11b4b5	160.7705
Au-GaN	D7t4t5	58.527	Au-GaN	D11b6b7	60.5932
Au-GaN	D8t3t5	35.2199	Au-GaN	D11t6t7	112.9118
Ti/Au-GaN	D10b1b2	2.3875	Au-GaN	D12t2b2	40.3259
Ti/Au-GaN	D10b3b4	17.2316	Au-GaN	D12t4b4	28.3412
Ti/Au-GaN	D10b5b6	17.2361	Au-GaN	D12t5b5	27.7265
Ti/Au-GaN	D10t1t3	36.396	Au-GaN	D12t6b6	21.9205
Ti/Au-GaN	D10t4t5	37.2209	Au-GaN	D12t7b7	36.0151

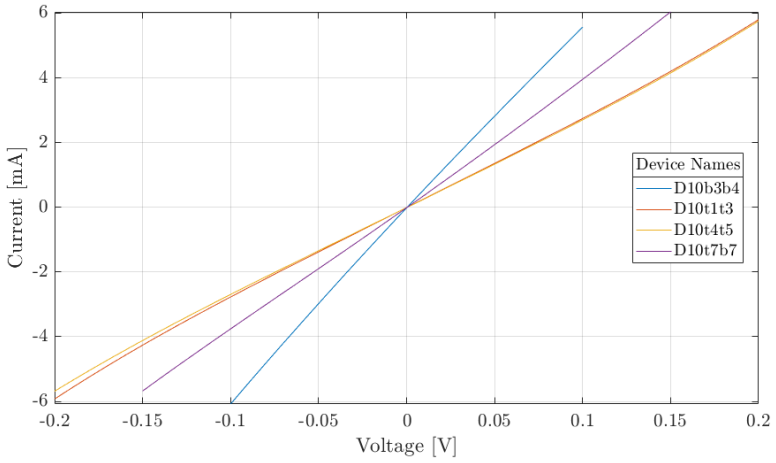

Figure 20: A graph showing the IV-characteristics of the least ohmic looking devices on D10.

ally for the measurements in the range $V \in [-0.05, 0.05]$ V. Most devices seem to have resistances on the order of a few 10 Ω, which is within reasonable limits.

4.3 Set-Up Development and Improvement

One of the goals of this study was to develop an experimental setup capable of measuring currents on the nA scale. This, of course, led to a multitude of challenges that needed to be overcome. As a consequence, before the design of the experimental apparatus in Figure 9 was finalised, there were several iterations of the apparatus tested, as well as a large number of component replacements and improvements made over time. Following this is a chronology of the development of this setup.

The IV measurement setup, shown in Figure 8, is what can only be considered the progenitor to the final setup in terms of cables, components and connectors. This initial setup is illustrated in Figure 21, and the potential flaws of this approach will be discussed in the following section.

In this first setup, the sample chip was connected to a breadboard held by a 3D-stage

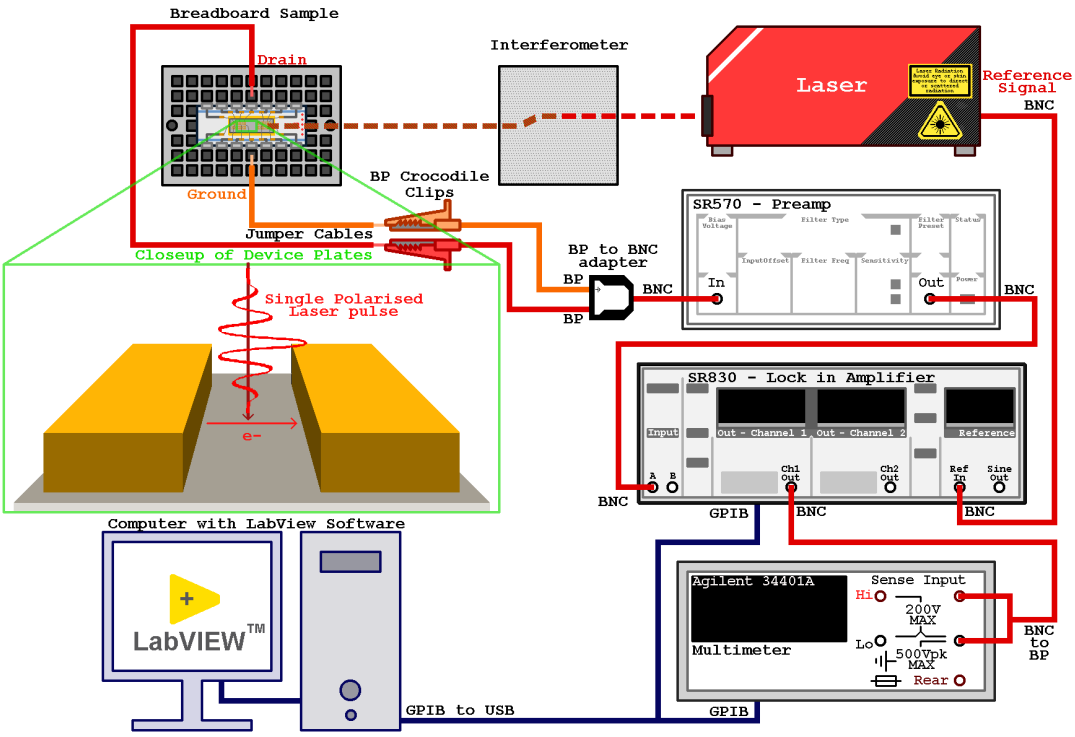

Figure 21: The initial setup used to measure the optical-field-induced currents in the two-colour experiments.

screwed onto a laser table. Unshielded jumper cables were connected to banana plug

cables by crocodile clips, later merged into the preamp via a double BP-to-BNC adapter. The same preamp, a Stanford Research Systems SR570, from the IV measurements was reused in this setup. Other than that, the rest of the setup is identical to the one shown in Figure 9. With this setup, the two-colour experiments were carried out. While there was a considerable amount of electronic noise present in these experiments, the noise floor was smaller than the largest measurable current. However, the noise floor for the ultrashort pulse experiments was higher than the signal, thus sources of noise, and the means to mitigate it needed to be found.

4.3.1 Sources of Noise and Steps Taken to Reduce it

Without proper shielding, nor grounding, every component before the preamp is highly susceptible to noise, and if not mitigated will also be amplified along with the signal itself, making it the most important source of noise to eliminate. Starting with the components shown in Figure 21, initial improvements were made without making major changes to it. First, the banana plug to BNC adapter was replaced with a grounding box in an attempt to mitigate the noise from the unshielded portion of the BP cables, it was later grounded to the power supply with copper grounding cables. On top of this, jumper cables do not have shielding, and neither do the ends of the crocodile clips that attach to them. Consequently, the full length of the wiring from the grounding box was wrapped in aluminium foil in attempt to mitigate the noise. After all of these combined efforts failed, it was clear that the setup itself needed changing.

First, all of the cables to and from the grounding box were fully replaced with high quality BNC cables, cut at the device facing end to connect to the breadboard. This resulted in some minor noise improvement. A larger issue, however, was caused by the lack of grounding on the laser table itself, and as such any cables in contact with, or near it, would introduce noise of an order of magnitude greater than if not. Furthermore, if the lights in the lab were turned off, the noise floor would sink considerably. This meant that any solution that reduces the length of cables, as well as prevents their close contact with the laser table, while also limiting the amount of light incident on the sample should reduce the noise considerably.

To solve most of these issues, a closed metal housing acting as a shielding box for the sample and the chip holder, as can be seen in Figure 9, was designed to reduce noise

picked up otherwise. This housing contains a breadboard, featuring a detachable lid and two BNC connectors, whose inside port have the ground and positive contact soldered to two short jumper cables cut at the ends. Its intent was to shield both the cable and its open ends, as well as the breadboard they connect to, whose metal connectors potentially act as antennas for stray signals. Furthermore, being an enclosed box, it also limits the incidence of external light sources, as well as providing a local ground in the case of the box.

While the shielding box did improve noise by an additional order of magnitude, it was discovered that simply having the sample mounted on the 3D stage added an additional order of magnitude of noise. It was initially thought that it was caused by contact to the metal post used to mount it to the stage, presumably due to the lack of grounding on the laser table. To ensure that it was fully separated from the laser table, a plastic cap was glued onto the side of the grounding box, which then was glued to the post. However, while the multimeter test to see if the stage and shielding box were fully insulated from one another showed that they were, elevated noise levels were still found when the shielding box was mounted on the 3D stage, generating about 0.2 mV of 100 μAV^{-1} amplified noise at all times. The source of this noise was not determined.

The biggest and most important improvement done to the set-up was the replacement of the pre-amplifier. The Femto DLCPA-200 preamp features a better amplification while preserving the bandwidth and was specifically designed for operation in electronically noisy laser laboratories. Its compact design allows for a placement close to the sample, reducing the length of any wiring and therefore resulting in a reduction of the set-up's overall susceptibility to electronic noise. These changes reduced the noise floor from several volts, down to just a few millivolts, and allowed for the signal to be distinguished using the reference signal from the laser in the lock-in amplifier.

4.4 Titanium-Sapphire Laser

Before experiments, the spot size of the laser focus was determined with a beam profiler. It varied, due to changes in the overall laser set-up, between 7 and 20 µm. The pulse duration of the laser pulses was determined using the d-scan technique[31] directly at the sample position. The pulses had a typical FWHM duration of 7 fs. The optical power was adjusted to reach the required intensities of $\sim 10^{13}$ Wcm^{-2} or, correspondingly, peak

field strength on the order of 0.5 VÅ^{-1}. This resulted in the usage of optical powers ranging from roughly 10 to 35 mW. While in initial experiments on pure gold contacts some sample damage could be observed, further improved fabrications were resistant to optical damage in this intensity regime. The Ti:Au contacts proved to be even more robust.

4.4.1 Current-Phase Measurements

For these experiments, computer-controlled wedges were moved to alter the CEP, after which the current was measured. Initial attempts were made to manually estimate the current at each wedge position, but the current fluctuated too broadly for a good estimate to be made. Consequently, a script was written to automatically measure the current at set phase increments by moving the fused silica wedges to alter it. The current is likely to fluctuate, so current measurements are integrated over 30 ms, in order to calculate a weighted average. Figure 22 shows a measurement taken from a, now damaged, Ti/Au-GaN device for when the lock-in mechanism is used, and not. The most important conclusion to draw from this is that the lock-in amplifier does produce more consistent results, even when the phase-locking is not working properly. It also appears that the decreasing current with increasing glass insertion matches directly what is observed, minus the complete sign inversion, in the modelled result from Figure 14(b), where increasing the

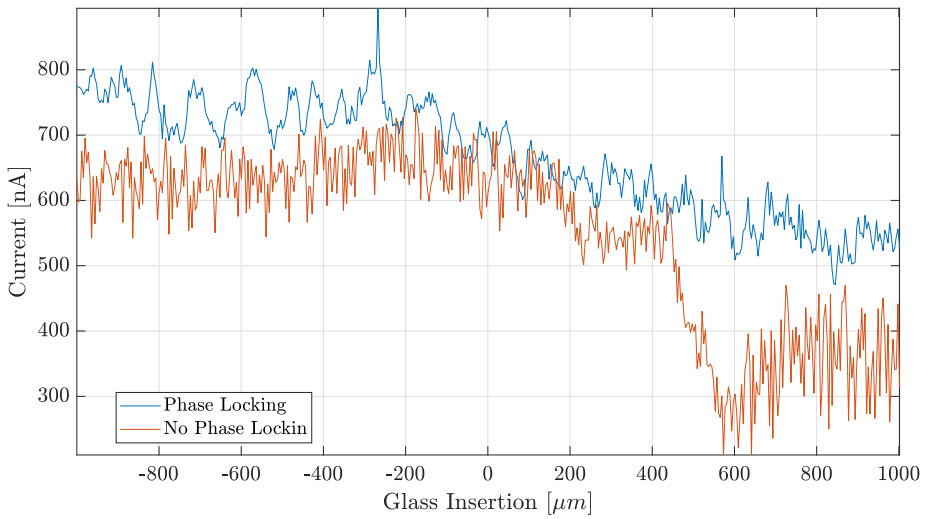

Figure 22: Two graphs showing the difference between the automated wedge-current measurements when using, and when not using, a lock in amplifier over a large range of different glass insertions. Note that these experiments were done when the setup had poor phase locking.

glass insertion increases the dispersion of the laser, consequently increasing the number of pulses and reducing the resultant vector potential momenta.

4.4.2 Current-Intensity Measurements

The power dependence is determined by measuring the voltage as a function of the optical power transmitted through a polariser pair. Table 4, and Figure 23, shows the manually determined power-voltage relation for Device 10, made with Ti/Au on GaN, for a range of laser powers. However, regardless of the polarisation of the laser, approximately the

Table 4: The measured power dependence from the Device 10, the Ti/Au GaN device fabricated using lift-off, from near minimum power, to maximum power.

Power [mW]	6	7	8	9	10	11	12	13	14	15	16	17	18	19.2
Voltage [mV]	0.27	0.48	0.74	1.37	1.9	3.1	4.6	6.7	8.8	12.6	15.9	20.0	23.4	26.6

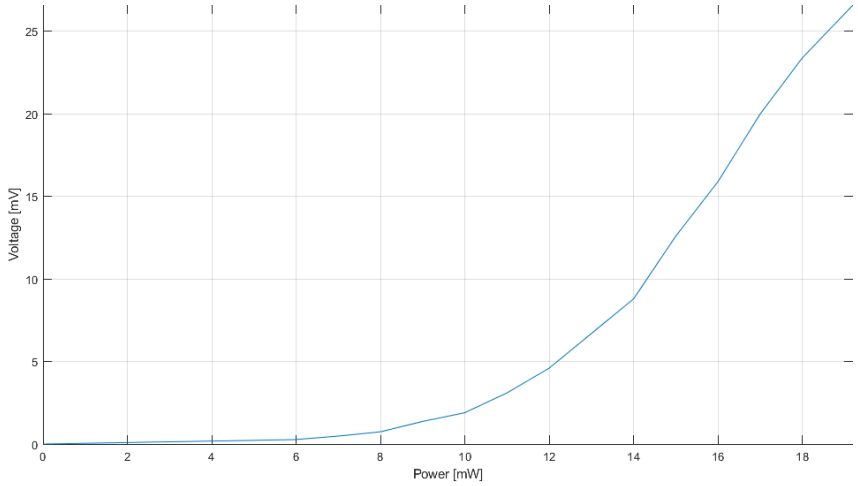

Figure 23: A graph plotting the measured power dependence listed in Table 4

same signal was measured. This is unfortunate, since no current is expected to be seen when the polarisation is parallel to the device plates. While, in this sample, there is a region down the area between the contacts where the carriers could exit, it should be too far for them to travel without recombining with the substrate. Note that, moving the laser spot from the region above, to the region below the contact, swaps the sign of the current. While this appears to support a polarisation dependence, since if the laser spot is above the contact, electrons are generated and travel down with the field to the contact, electrons travel away. The inconsistency in findings leaves this unsolved for now.

4.5 Ytterbium Laser

Measurements from the Yb laser confirmed the polarisation dependence of the current direction. In addition to this, a single long scan, measuring the current over a large range of pulse delays, was obtained. Although, while some interesting observations could be made from the scan, these experiments yielded no real usable data, since the laser would rapidly destroy the devices when they were being measured.

4.5.1 Two-Colour Current Measurement

With a long pulse high power laser, there should have been no issue generating a two-colour overlap whose vector potential was sufficiently large to generate optical-field-induced currents, as previously demonstrated in the model. In spite of the destructive properties of the laser, currents were observed with the correct expectation that its sign would change depending on the polarisation of the laser.

When software was written to automatically move the stage in order to alter the Δt of the two pulses to measure the current at varying pulse delays, the measurements, plotted in Figure 24, do not appear to follow the trend expected. Instead of observing an oscillation akin to Figure 16, a low baseline current can be seen, with several high current plateaus, each appearing to instantaneously decay back to the baseline after some time. Note that the small oscillations are an artefact from the setup, they were present even without laser incidence. It was proposed that perhaps some impurity in the device was being charged, allowing for a higher current during discharge. Alternatively, since

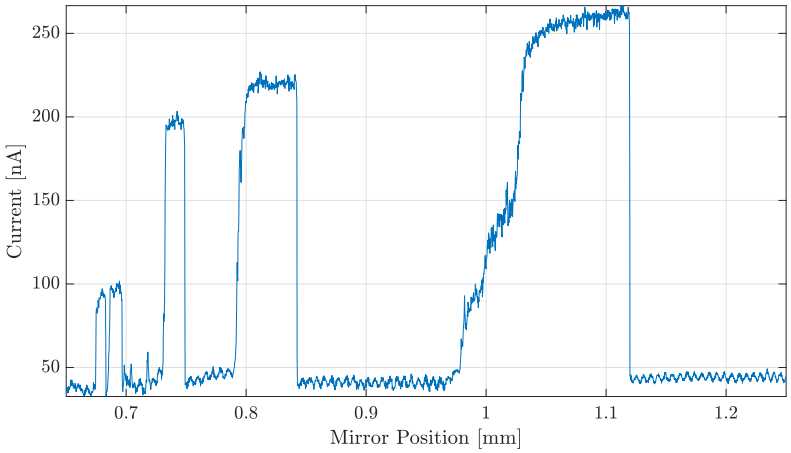

Figure 24: Current measurements over a large range of mirror positions, whose position determines the relative delay of the second harmonic from the fundamental.

the Yb laser would quickly destroy the devices, perhaps the gradual degradation of the Au contacts led to the creation of plasmonic hotspots, generating a current during laser incidence. The source of this could not be determined.

4.6 The Effects of High Intensity Laser Exposure

Unfortunately, the incidence of especially high intensity laser pulses will eventually damage the devices. Thus was especially evident from the two-colour superposition experiments using the Yb laser, where damage would be visible to the naked eye within seconds, even at relative low power for that system. Some damage would eventually also be generated after prolonged high intensity exposure from the Ti:Sa laser, but not nearly as quickly, nor as severe as the Yb laser. Figure 25 shows a selection of laser damage done by both the Yb laser, and the Ta:Sa.

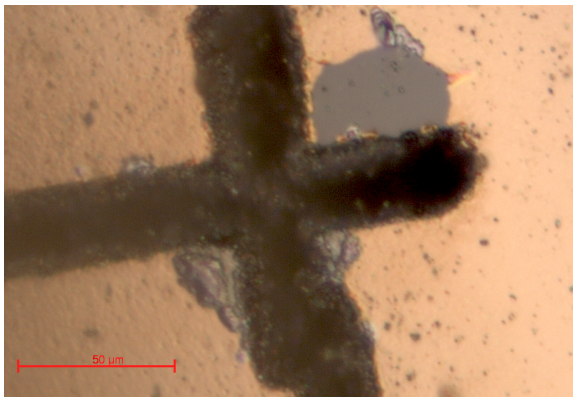

(a) Close-up of damage to Au on GaN

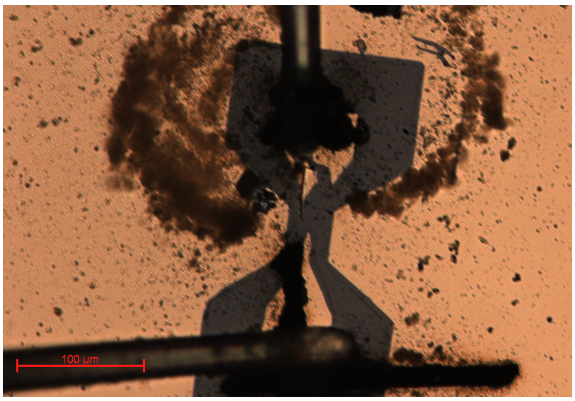

(b) A close-up of a damaged Au-GaN device

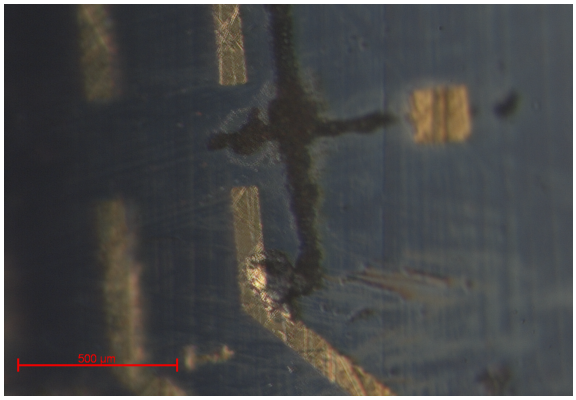

(c) Damage to SiO_2 and Ti/Au contacts

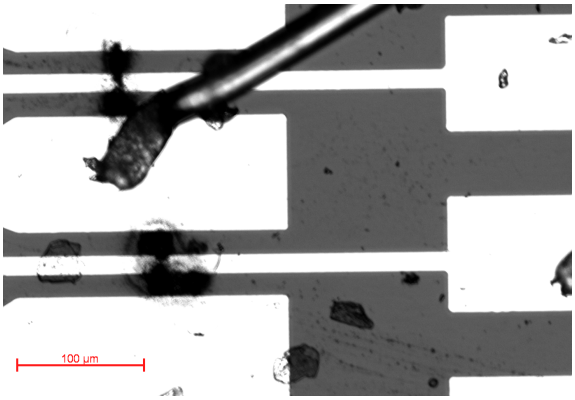

(d) Damaged Ti/Au-GaN device contacts

Figure 25: Four images showing laser damaged devices. (a) to (c) show devices damaged by the Yb laser, and (d) shows damage from extended high intensity exposure to the Ti:Sa laser. The Yb laser burnt clean through both Au and GaN, while being less damaging to the Ti/Au-SiO_2 device.

5 Discussion

This study has seen the full reproduction of the quantum interference model proposed by Khurgin, in addition to expanding on its functionality and writing a versatile system that automates a large portion of the work required to calculate and plot the results. The direct parallels that the model has to the device measurements in both set ups should have allowed the experimental results to be directly compared to the model. The importance of comparing the results from the model using variables that correspond to the different experimental setups used would allow for confirmation, assuming the model fits the measurements, that Khurgin's model is not overfitting to the data it bases its model on.[9] [1] If it is so that this model can be applied to correctly predict the measurements resulting from different laser systems and device architectures, then it adds considerable weight to the proposition that the optical-field-induced currents are a result of quantum interference instead of any of the other four proposed models.

Due to the lengthy setup development time, much has been learned about that conditions that need to be met to measure small currents in an otherwise electronically noisy setting. Even with a lock in amplifier, whose sole purpose is to only pick up signals whose frequency matches that of a given reference signal, any noise that distorts the original signal will also be picked up. Any cable, unshielded or no, carrying any part of the signal is susceptible to crosstalk with other cables carrying a signal with the same carrier frequency. Sources of noise experienced in the lab due to this include the source and drain cables, the cables near the preamp, a power strip near the setup and even the reference signal to the lock in. At the end of the development, the source was terminated, first by a 50 Ω resistor, and then grounded to the shielding box. Since the Femto preamp could be placed directly on the laser table, any potential crosstalk between stray cables from the sample to the preamp would have been eliminated. There are still several improvements that could be made, but many solutions would require a different lab environment.

5.1 Potential Improvements

The laser table used for the experiments did not have ample room for a large setup, thus many compromises had to be made. The final focusing mirror before the device sample needed to have a very short focal length in order to focus the laser into a small enough

spot. This had an unintended side effect of limiting the use of the shielding box, namely preventing the use of its lid. When screwed on, the lid would prevent the sample from being moved into the focal point of the laser, since the lid would have collided with the mirror if the sample was moved into the focal point of the laser. Without it, the shielding box cannot fully protect the sample from external light, and doesn't fully prevent all noise that it would have otherwise, if fully sealed. An improvement would have been if the laser focusing setup could have been built elsewhere, allowing the shielding box lid to be used. In addition to this, even though the shielding box was completely insulated from the 3D stage, some noise was still introduced when mounted. Identifying and mitigating the source of this noise would have greatly improved the signal quality.

While the effect, if any, of plasmonic hotspots could not be confirmed in detail, utilising an EBL system to develop devices should have, in theory, reduced their effect with more well defined, and smoother edges. In addition to this, EBL fabrication allows for an easier and more flexible implementation of custom device designs, improving the ease of designing, and testing, new device designs. For instance, the only condition for devices in this study was for there to be two well-defined, parallel contacts, separated by only a few microns. Thus, having a central contact with several contacts with edges parallel to the central one would require only wiring bonding to a two areas for several devices, instead of two per device. An mock-up of such a device design can be seen in Figure 26. This type of design would be useful to do further experiments with highly destructive lasers, like the Yb laser. It would greatly reduce the time spent wire bonding new devices after destroying old ones with the laser. Furthermore, since it would have to be made using EBL, it will also have a higher success rate, at the expense of a lengthier fabrication

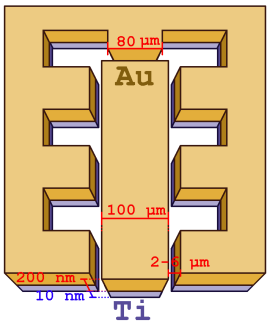

Figure 26: A mock-up device design that creates several device areas from only a two contacts. This device design could be made using EBL.

process, and would allow for Ti/Au contacts, since it is not limited by any etchant, but instead uses lift-off as the final step.

Since the CEP of the laser drifts over time, requiring readjustment every hour or so, one of the key means to improve results is to increase the speed of measurement acquisition. Even though, initially, most of the measurements were done by hand, eventually automated systems were created to handle longer scans. Writing a new system that can take several scans one after the other, to then average same parameter results, may produce better results, and limit the problems caused by drift.

5.2 Sources of Error

There are many sources of error that must be taken into consideration when attempting to make conclusions from the results. The biggest source of uncertainty, by far, was the large amount of electrical noise present in most of the measurements. When attempting to measure the power dependence, the maximum power of the laser would give a signal that fluctuated by about 3 mV up and down from a median of about 25 mV, an error term nearly 12% as large as the measurement itself. Note that greater laser powers generated a greater fluctuation, and that lower laser powers did not have nearly as large fluctuations. Further attempts to reduce noise would have first had to identify the source of this, seemingly regular interval of, current fluctuation.

Another big difficulty came from the correct focus and alignment of the laser spot to the device area. Not only did the transparent GaN make it difficult to distinguish the spot on the surface from the one on the chip itself, but properly aligning the spot with only the camera proved difficult. An out-of-focus position on the sample would see a too low laser intensity to generate any optical-field-induced currents, and a misaligned laser would give no reading. Alternatively, plasmonic hotspots, especially on devices with a small distance between contacts, could generate a current in the gold with the laser spot aligned to an edge instead, leading to the detection of a current with a matching carrier frequency not related to any optical-field-induced currents. Since these signals would be otherwise indistinguishable, a good alignment to the device area is imperative, else there is no guarantee that the measured current comes as a result of the optical-field-induced currents, or not. An additional factor to consider, is that the laser polarisation had to be matched with the junction.

The wire bonding process is also prone to error, especially with the samples that have very small contacts. A few devices ended up accidentally connecting together neighbouring gold pads, and in some cases a current could be measured in all devices simultaneously from a, possibly, shared contact. In addition to this, GaN is particularly difficult material to wire bond to, since it is transparent, making it difficult to determine where exactly on the surface the gold contacts are. A solution to this would have been to use an opaque material substrate or, like the SiO_2 samples used, one that has an opaque surface oxide. While it should be possible to determine if the wire bonding was successful from the IV curves, the substrate materials used were highly doped, and as such gave near metallic IV-curves. Thus, distinguishing between good and bad devices was difficult. The gap between the contacts should act as a potential barrier, as such ideal devices should have IV curves that show more diode-like characteristics, unlike many that were used for the experiments.

While gold etching is a time effective method to produce a lot of devices, a poorly made sample is not immediately evident. Since it cannot use titanium as an adhesion layer, it must rely fully on the gold to make a good contact with the substrate. If the sample is overetched, then gold may have a large overhang which, when wire bonded to, could collapse to make for an ineffective connection to the substrate. As has been seen already, it is also possible for gold to suffer adhesion failure, where it fully detaches from the substrate. Lift-off, on the other hand, does not have this problem, since it allows for Ti/Au contacts to be made, where Ti acts as an adhesion layer. A downside, however, is that it does give more rough edge definition, which may cause current generation by plasmonic hotspots. There are advantages and disadvantages to both methods, but since the only measured currents come from the one Ti/Au device fabricated, further device testing needs to be done before any conclusions on which fabrication method is preferable.

5.3 Conclusions and Outlook

In this project, a setup capable of measuring optical-field-induced currents in the nA regime was successfully developed from an initial concept that was incapable of distinguishing noise from signal. The breadth of noise sources that were identified and eliminated cannot be understated, especially when the characteristics of much of it shared the same frequency as the signal. While, unfortunately, many of the modelled results could not

be measured experimentally, and thus could not be compared directly, a few important results were made. The brief experiments using the Yb laser, however damaging it may have been to the devices, directly proved that the direction of optical-field-induced currents was dependent on the polarisation of the laser. This is but one piece of evidence supporting the proposed quantum interference means of directional current generation. From the Ti:Sa laser, a current was eventually observed in the Ti/Au-GaN devices. More importantly, the automated glass insertion-current measurements did show a decreasing current with an increased glass insertion, akin to what was observed in the model, but this was more likely simply due to the laser intensity being reduced by the dispersive medium. Future experiments, however, are very promising. Should a faster measurement acquisition method be created such that results can be gathered faster than the phase locking on the laser can drift, then this setup has a great potential to measure the optical-field-induced currents. A goal for the near future would therefore be to also observe a phase dependence using the Ti:Sa laser.

A large number of devices were fabricated for this study. As an initial conclusion, since no currents could be measured from any of the devices made using gold etching on the Ti:Sa setup, future devices should all be made using lift-off, to ensure that a Ti adhesion layer can be deposited, improving the surface contact with the substrate and thus device turnout. What would be especially interesting is for the use of more durable substrate materials, so that better measurements could be measured from the Yb laser. The ideal case would be to move towards using only EBL for device masking, allowing for custom designs tailored to the ideal conditions for optical-field-induced currents to be generated by incident laser pulses. Furthermore, investigations into non-refractory contact materials would be required to fully exclude the possibility that the currents observed were not generated by plasmonic hotspots.

Finally, the GUI written for the reproduction of Khurgin's model has made possible the quick generation of experimental predictions, and could easily be expanded to include a feature that can import experimental results, and attempt to fit the model to it. It could be made a valuable analysis tool for the future.

References

[1] J. B. Khurgin, "Optically induced currents in dielectrics and semiconductors as a nonlinear optical effect," *J. Opt. Soc. Am. B*, vol. 33, no. 7, pp. C1–C9, Jul 2016. [Online]. Available: http://josab.osa.org/abstract.cfm?URI=josab-33-7-C1

[2] G. Kurizki, M. Shapiro, and P. Brumer, "Phase-coherent control of photocurrent directionality in semiconductors," *Phys. Rev. B*, vol. 39, pp. 3435–3437, Feb 1989. [Online]. Available: https://link.aps.org/doi/10.1103/PhysRevB.39.3435

[3] E. Dupont, P. B. Corkum, H. C. Liu, M. Buchanan, and Z. R. Wasilewski, "Phase-controlled currents in semiconductors," *Phys. Rev. Lett.*, vol. 74, pp. 3596–3599, May 1995. [Online]. Available: https://link.aps.org/doi/10.1103/PhysRevLett.74.3596

[4] R. Atanasov, A. Haché, J. L. P. Hughes, H. M. van Driel, and J. E. Sipe, "Coherent control of photocurrent generation in bulk semiconductors," *Phys. Rev. Lett.*, vol. 76, pp. 1703–1706, Mar 1996. [Online]. Available: https://link.aps.org/doi/10.1103/PhysRevLett.76.1703

[5] A. Haché, Y. Kostoulas, R. Atanasov, J. L. P. Hughes, J. E. Sipe, and H. M. van Driel, "Observation of coherently controlled photocurrent in unbiased, bulk GaAs," *Phys. Rev. Lett.*, vol. 78, pp. 306–309, Jan 1997. [Online]. Available: https://link.aps.org/doi/10.1103/PhysRevLett.78.306

[6] H. Zhao, E. J. Loren, H. M. van Driel, and A. L. Smirl, "Coherence control of hall charge and spin currents," *Phys. Rev. Lett.*, vol. 96, p. 246601, Jun 2006. [Online]. Available: https://link.aps.org/doi/10.1103/PhysRevLett.96.246601

[7] D. A. Bas, K. Vargas-Velez, S. Babakiray, T. A. Johnson, P. Borisov, T. D. Stanescu, D. Lederman, and A. D. Bristow, "Coherent control of injection currents in high-quality films of Bi2Se3," *Applied Physics Letters*, vol. 106, no. 4, p. 041109, 2015. [Online]. Available: https://doi.org/10.1063/1.4907004

[8] E. Sternemann, T. Jostmeier, C. Ruppert, H. T. Duc, T. Meier, and M. Betz, "Femtosecond quantum interference control of electrical currents in GaAs: Signatures

beyond the perturbative $\chi^{(3)}$ limit," *Phys. Rev. B*, vol. 88, p. 165204, Oct 2013. [Online]. Available: https://link.aps.org/doi/10.1103/PhysRevB.88.165204

[9] A. Schiffrin, T. Paasch-Colberg, N. Karpowicz, V. Apalkov, D. Gerster, S. Mühlbrandt, M. Korbman, J. Reichert, M. Schultze, S. Holzner, J. V. Barth, R. Kienberger, R. Ernstorfer, V. S. Yakovlev, M. I. Stockman, and F. Krausz, "Optical-field-induced current in dielectrics," *Nature*, vol. 493, pp. 70 EP –, Dec 2012. [Online]. Available: http://dx.doi.org/10.1038/nature11567

[10] T. Paasch-Colberg, S. Y. Kruchinin, Özge Sağlam, S. Kapser, S. Cabrini, S. Muehlbrandt, J. Reichert, J. V. Barth, R. Ernstorfer, R. Kienberger, V. S. Yakovlev, N. Karpowicz, and A. Schiffrin, "Sub-cycle optical control of current in a semiconductor: from the multiphoton to the tunneling regime," *Optica*, vol. 3, no. 12, pp. 1358–1361, Dec 2016. [Online]. Available: http://www.osapublishing.org/optica/abstract.cfm?URI=optica-3-12-1358

[11] O. Kwon, T. Paasch-Colberg, V. Apalkov, B.-K. Kim, J.-J. Kim, M. I. Stockman, and D. Kim, "Semimetallization of dielectrics in strong optical fields," *Scientific Reports*, vol. 6, pp. 21 272 EP –, Feb 2016, article. [Online]. Available: https://doi.org/10.1038/srep21272

[12] J. D. Lee, W. S. Yun, and N. Park, "Rectifying the optical-field-induced current in dielectrics: Petahertz diode," *Phys. Rev. Lett.*, vol. 116, p. 057401, Feb 2016. [Online]. Available: https://link.aps.org/doi/10.1103/PhysRevLett.116.057401

[13] I. Franco, M. Shapiro, and P. Brumer, "Robust ultrafast currents in molecular wires through stark shifts," *Phys. Rev. Lett.*, vol. 99, p. 126802, Sep 2007. [Online]. Available: https://link.aps.org/doi/10.1103/PhysRevLett.99.126802

[14] T. Mueller, F. Xia, and P. Avouris, "Graphene photodetectors for high-speed optical communications," *Nature Photonics*, vol. 4, pp. 297 EP –, Mar 2010. [Online]. Available: https://doi.org/10.1038/nphoton.2010.40

[15] L. Prechtel, L. Song, S. Manus, D. Schuh, W. Wegscheider, and A. W. Holleitner, "Time-resolved picosecond photocurrents in contacted carbon nanotubes," *Nano Letters*, vol. 11, no. 1, pp. 269–272, 2011, pMID: 21142051. [Online]. Available: https://doi.org/10.1021/nl1036897

[16] F. Krausz and M. I. Stockman, "Attosecond metrology: from electron capture to future signal processing," *Nature Photonics*, vol. 8, pp. 205 EP –, Feb 2014, review Article. [Online]. Available: http://dx.doi.org/10.1038/nphoton.2014.28

[17] K. Ahi, "Review of GaN-based devices for terahertz operation," *Optical Engineering*, vol. 56, pp. 56 – 56 – 14, 2017. [Online]. Available: https://doi.org/10.1117/1.OE.56.9.090901

[18] T. Higuchi, C. Heide, K. Ullmann, H. B. Weber, and P. Hommelhoff, "Light-field-driven currents in graphene," *Nature*, vol. 550, pp. 224 EP –, Sep 2017. [Online]. Available: https://doi.org/10.1038/nature23900

[19] C. Heide, T. Higuchi, H. B. Weber, and P. Hommelhoff, "Coherent electron trajectory control in graphene," *Phys. Rev. Lett.*, vol. 121, p. 207401, Nov 2018. [Online]. Available: https://link.aps.org/doi/10.1103/PhysRevLett.121.207401

[20] A. Schiffrin, T. Paasch-Colberg, N. Karpowicz, V. Apalkov, D. Gerster, S. Mühlbrandt, M. Korbman, J. Reichert, M. Schultze, S. Holzner, J. V. Barth, R. Kienberger, R. Ernstorfer, V. S. Yakovlev, M. I. Stockman, and F. Krausz, "Addendum: Optical-field-induced current in dielectrics," *Nature*, vol. 507, pp. 386 EP –, Mar 2014, addendum. [Online]. Available: https://doi.org/10.1038/nature13077

[21] S. Y. Kruchinin, M. Korbman, and V. S. Yakovlev, "Theory of strong-field injection and control of photocurrent in dielectrics and wide band gap semiconductors," *Phys. Rev. B*, vol. 87, p. 115201, Mar 2013. [Online]. Available: https://link.aps.org/doi/10.1103/PhysRevB.87.115201

[22] L. Chen, Y. Zhang, G. Chen, and I. Franco, "Stark control of electrons along nanojunctions," *Nature Communications*, vol. 9, no. 1, p. 2070, 2018. [Online]. Available: https://doi.org/10.1038/s41467-018-04393-4

[23] *PHYS370 - Advanced Electromagnetism.* University of Liverpool, ch. Part 2: Electromagnetic Waves in Dielectric Media.

[24] R. Trebino, "Ultrashort laser pulses I," accessed on 2018-11-02. [Online]. Available: https://www.brown.edu/research/labs/mittleman/sites/brown.edu.research.labs.

mittleman/files/uploads/lecture6_0.pdf

[25] https://www.newport.com/n/the-effect-of-dispersion-on-ultrashort-pulses, accessed on 2018-10-03.

[26] J. Diels and W. Rudolf, *Ultrashort Laser Pulse Phenomena, Second Edition.* Massachusetts, Academic Press, 2006.

[27] E. Coadou, "A coherent technical note - propagation, dispersion and measurement of sub-10 fs pulses," https://edge.coherent.com/assets/pdf/COHR_WP_PropagationDispersionMeasurement_of_sub_10fsPulses_08_29_18.pdf, accessed on 2019-03-15.

[28] R. Paschotta, "Article on 'chromatic dispersion' in the rp photonics encyclopedia," https://www.rp-photonics.com/chromatic_dispersion.html, accessed on 2018-10-03.

[29] J. Liang, F. Kohsaka, T. Matsuo, X. Li, and T. Ueda, "Improved bi-layer lift-off process for mems applications," *Microelectronic Engineering*, vol. 85, no. 5, pp. 1000 – 1003, 2008, proceedings of the Micro- and Nano-Engineering 2007 Conference. [Online]. Available: http://www.sciencedirect.com/science/article/pii/S0167931708001160

[30] A. Harth, C. Guo, Y.-C. Cheng, A. Losquin, M. Miranda, S. Mikaelsson, C. M. Heyl, O. Prochnow, J. Ahrens, U. Morgner, A. L'Huillier, and C. L. Arnold, "Compact 200 kHz HHG source driven by a few-cycle OPCPA," *Journal of Optics*, vol. 20, no. 1, p. 014007, dec 2017. [Online]. Available: https://doi.org/10.1088%2F2040-8986%2Faa9b04

[31] M. Miranda, C. L. Arnold, T. Fordell, F. Silva, B. Alonso, R. Weigand, A. L'Huillier, and H. Crespo, "Characterization of broadband few-cycle laser pulses with the d-scan technique," *Opt. Express*, vol. 20, no. 17, pp. 18 732–18 743, Aug 2012. [Online]. Available: http://www.opticsexpress.org/abstract.cfm?URI=oe-20-17-18732

[32] V. Flodgren. Quint-optofieldcharge. [Online]. Available: https://github.com/DeltaMod/QuInt-Optofieldcharge

[33] M. N. Polyanskiy, "Refractive index database," https://refractiveindex.info, accessed on 2018-10-03.

Appendix A - Matlab Model Implementation

Proper Integral Handling in Matlab

Note that, when calculating the integral under $a(t)$ using computer software, it is best calculated using a function that estimates the known area using a trapezoidal estimate, like `trapz(x,y)`. For instance, if MATLAB is asked to calculate the integral of:

$$\texttt{funE\_t} = @(\texttt{time}, \texttt{T}, \texttt{n}, \texttt{w\_0})(\exp(-2 * \log(2). * ((\texttt{t} - \texttt{t\_0})/\texttt{T}).\texttt{\^{}}2). * \cos(\texttt{w\_0x} * (\texttt{t} - \texttt{t\_0})))$$

$$\langle \texttt{a\^{}2n} + 1 \rangle = \texttt{w\_0} * \texttt{integral}(@(\texttt{time})\texttt{funE\_t}(\texttt{time}, \texttt{T}, \texttt{n}, \texttt{w\_0}), -\texttt{inf}, \texttt{inf})$$

then it estimates it to be equal to zero, since the majority of evaluated points are zero. Choosing to set 'Waypoints' requires defining every single point contained in the time vector t, meaning that a more computationally intensive process eventually uses the same trapezoidal estimate as the function `trapz(t,E_t)`.

Plotting $\langle \mathbf{a^{2n+1}} \rangle$ for more $\mathbf{N_{cyc}}$

Figure 11b only shows Equation (24) plotted up to $N_{cyc} = 3.5$. To show why, an expanded range of $N_{cyc} \in [0, 50]$ is used to calculate new values of $\langle a^{2n+1} \rangle$. With this comes the requirement of a larger time axis, so that integral is evaluated fully, the same goes for the number of sampling points, as to eliminate low sample rate errors. Figure 27 shows this much expanded range of vector potential momenta values. As is evident from the figure, at $N_{cyc} > 4$ the vector potential momenta becomes negligibly small. It is at this point that the laser pulse has a waveform that, overall, is symmetric enough to have no resultant vector potential from the pulse other than the strength of the electric field. The fluctuations seen past this are on the order of 10^{-17} to 10^{-15}.

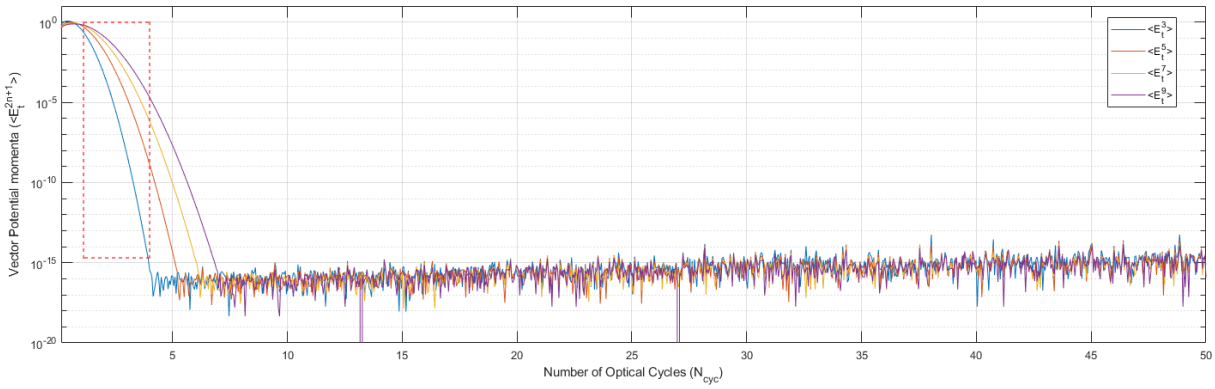

Figure 27: Expanded version of Figure 11b (indicated by the red dotted square) showing the vector potential momenta $\langle a^{2n+1} \rangle$ calculated for values of $N_{cyc} \in [0, 50]$. 2000 different laser pulses are evaluated for each of the four odd powers of $E(t)^{2n+1}$, generated per value N_{cyc}. Each integral is determined using a trapezoidal estimate containing 300000 sample points.

Efficient Dispersion Application

There is no convenient way to Fourier-transform a dataset, apply dispersion, and then transform it back. In writing the code, a function called `FFTD` was written specifically to handle this process, amongst many others.[32]

```
%%This function is written to handle transforms to, and application of
% dispersion between time and frequency domain.
%
%-----------------------------------------USAGE-----------------------------------------%
%                        A = FFTD(x,y,w_0,'type',Phi,Theta)
% x is your x axis (time or frequency axis, select a proper type to match)
%
% y is your intensity/amplitude
%
% 'type' is a string that indicates which transform you want to do:
%                           |  ttf = time to frequency   |
%                           |  ttt = time to time        |
%                           |  ftt = frequency to time   |
%
%-------------------------------External Variables--------------------------------%
% Theta, is a single value phase shift in the time domain. Set to 0 usually
%
% Phi is a 4 length vector containing phi_0, phi_1, phi_2, phi_3. You can
% define them as (x,y[phi_0,phi_1,phi_2,phi_3])
%
% phi_0 changes pulse phase, phi_1 changes pulse time "location",
% phi_2 changes pulse width, phi_3 alters pulse shape in time
%
%
%
%-------------------------------Output Format--------------------------------%
%
% All variables will be in A, as per: [A] = FFTD(x,y,w_0,'type',Phi,Theta)
% the actual output will be given as:
% A.type.variable - e.g. A.ttt.Et, gives the non dispersed time axis in the
% type = ttt, time to time dispersion. For the dispersion, you must write
% A.ttt.Etdisp. The same logic goes for all variables:
%  ------------------------------------------------------------------------------%
%  | A.ttf.Et & A.ttf.t | A.ttf.Ew & A.ttf.w |                                 |
%  |--------------------|--------------------|---------------------------------|
%  | A.ttt.Et & A.ttt.t | A.ttt.Ew & A.ttt.w | A.ttt.Etdisp & A.ttt.tdisp|
%  |--------------------|--------------------|---------------------------------|
%  |                    | A.ftt.Ew & A.ftt.w | A.ftt.Etdisp & A.ftt.tdisp|
%  ------------------------------------------------------------------------------
% Note: using ftt assumes you've already applied dispersion. Inputting Phi
```

```
41 % is just to print PHITEXT, and keep track of which dispersion you used!
42 function A = FFTD(x,y,w_0,type,Phi,Theta)
43 %% --- Variables --- %%
44 if issorted(real(y)) == 1
45 fprintf(2,['ERROR: Your "y" input is a sorted vector. ',...
46 'Are you sure you`ve not accidentally given your time/frequency axis? \n',...
47 '       If this is not the case, change issorted(y) to == 0 \n'])
48 else
49 if mean(strcmp(type,{'ttt';'ttf';'ftt'})) > 0
50 %Temporal Variables
51 A.N    = length(x);                                    % N length vector
52 A.t    = x;                                            % Time Axis
53 A.t1   = A.t(1); A.t2 = A.t(end);                      % Start and end time
54 A.t_0  = mean(A.t);                                    % Centre Time Axis (
       mean of axis)
55 A.Dt   = (A.t(end) - A.t(1));                          % Sampling interval
56 A.dt   = A.Dt/A.N ;                                   % Smallest Time
       interval
57 A.w_t1 = 2*pi()/A.Dt; A.w_t2 = 2*pi()/A.dt;          % Min-Max Frequency
       from time graph
58
59 %Frequency Variables
60 A.w    = x;                                            % Frequency Axis (iff
       type = ftt)
61 A.w_0  = w_0;                                          % Centre Frequency
62 A.w1 = A.w(1); A.w2 = A.w(end);                        % Highest/Lowest Freq
63 A.Dw   = A.w2 - A.w1;                                  % Frequency Difference
64 A.dw   = A.Dw/A.N;                                    % Smallest Frequency
       inverval
65 A.Dt_w = 2*pi()/A.w1; A.dt_w = 2*pi()/A.w2;          % Determining Max/min
       time interval from frequency
66 A.t_w1 = -A.Dt_w/2; A.t_w2 = A.Dt_w/2;               % Determining time axis
        start/end variables
67
68
69 fun_theta = @(theta) theta*pi();                                    %
       This sets phase offset
70 fun_phiw = @(phi0, phi1, phi2, phi3,w,w_0)      phi0                +... %
       phi_0 is Carrier Envelope Phase - Values of pi()
71 phi1.*((w-w_0))         +...  %phi_1 is the Group Delay
72 phi2.*((w-w_0).^2)/2    +...  %phi_2 is the Group Velocity Dispersion GVD
73 phi3.*((w-w_0).^3)/6 ;        %phi_3 is the Third Order Dispersion
74 A.phi = Phi;                                                       %
       Get \phi values in a struct
75 A.phiw = fun_phiw(A.phi(1), A.phi(2), A.phi(3), A.phi(4),A.w,A.w_0);    %
       Get dispersion factor
```

```
76 A.theta = fun_theta(Theta);                                          %
       Get phase offset
77
78 %% Calculate post dispersion delay, and how many units to shift the pulse
       by to center it %
79 A.tD    = A.phi(2); % The added time delay by phi_2
80 A.tcirc = round(A.N*(round(A.phi(2)/A.Dt)-A.phi(2)/A.Dt));
81 end
82 switch type
83
84 case 'ttf'
85 %% ------ E_t -> E_w ------ %%
86 %Getting Axis Variables
87 A.ttf.Et = y;                          % Get E(t)
88 A.Et = y/max(y);                       % Normalise E(t) to a(t)
89 A.ttf.t = x;                           % Get time axis
90
91 % Perform fft and add dispersion
92 A.Etfft=fft(A.Et);                      % fft with no padding
93 A.wfft =linspace(A.w_t2,A.w_t1,A.N); % Defining the frequency axis - it's "
       backwards" because the fft goes high to low freq
94 A.ttf.w = A.wfft;                      % Get frequency axis
95 A.Etfft = A.Etfft.*exp(-1i.*fun_phiw(A.phi(1),A.phi(2),A.phi(3),A.phi(4),A.
       wfft,A.w_0)); %Apply dispersion
96 A.ttf.Ew = A.Etfft;
97 % Save text of which dispersion factor was used, useful for legend entries
98 A.ttf.PHITEXT = sprintf(['\\phi_0 = ', num2str(A.phi(1),'%.4g'),'\n',...
99 '\\phi_1 = ', num2str(A.phi(2),'%.4g'),'\n',...
100 '\\phi_2 = ', num2str(A.phi(3),'%.4g'),'\n',...
101 '\\phi_3 = ', num2str(A.phi(4),'%.4g'),'\n']);
102
103 case 'ttt'
104 %% ------ E_t -> E_w ------ %%
105 %Getting Axis Variables
106 A.ttt.Et = y/max(y);                   % Get E(t)
107 A.Et = y/max(y);                       % Normalise E(t) to a(t)
108 A.ttt.t = x;                           % Get time axis
109
110 % Perform fft and add dispersion
111 A.Etfft=fft(A.Et);                      % fft with no padding
112 A.wfft =linspace(A.w_t2,A.w_t1,A.N); % Defining the frequency axis - it's "
       backwards" because the fft goes high to low freq
113 A.ttt.w = A.wfft;                      % Get frequency axis
114 A.Etfft = A.Etfft.*exp(-1i.*fun_phiw(A.phi(1),A.phi(2),A.phi(3),A.phi(4),A.
       wfft,A.w_0)); %Apply dispersion
115 A.ttt.Ew = A.Etfft;                    % Get E_w(t) = fft(E_t(t))
116
```

```
117 %% ---- E_w -> E_t ---- %%
118 A.Etifft =flip((ifft(A.Etfft)));    %We flip Ew before ifft, because
        otherwise it is backwards when transformed back
119 Dt = 2*pi()/A.wfft(end); dt_w = 2*pi()/A.wfft(1); %Extract max/min time
120 t1 = -A.t_0; t2 = Dt-A.t_0;          % Set t1/t2
121 A.t_ifft = linspace(t1,t2,A.N);      % Get time axis
122 A.ttt.Etdisp = A.Etifft;             % Get dispersed Et
123 A.ttt.tdisp  = A.t_ifft;             % Get new time axis (ideal case, is the
        same as input)
124 A.ttt.Etdispc = circshift(A.Etifft,A.tcirc); % Central pulse
125 A.ttt.tdispc  = A.ttt.tdisp + A.tD;          % Time shifted axis - for
        centralised pulse
126 % Save text of which dispersion factor was used, useful for legend entries
127 A.ttt.PHITEXT = sprintf(['\\phi_0 = ', num2str(A.phi(1),'%.4g'),'\n',...
128 '\\phi_1 = ', num2str(A.phi(2),'%.4g'),'\n',...
129 '\\phi_2 = ', num2str(A.phi(3),'%.4g'),'\n',...
130 '\\phi_3 = ', num2str(A.phi(4),'%.4g'),'\n']);
131
132 case 'ftt'
133 %% ---- E_w -> E_t ---- %%
134 %Getting Axis Variables
135 A.ftt.w  = x;         % Get frequency axis
136 A.ftt.Ew = y/max(y); % Get normalised frequency domain
137 A.Ew     = y/max(y); %Note: The current Ew equation includes the phi
        component, so you must change that to apply a different dispersion.
138
139 % Perform ifft
140 A.Ewfft      = fftshift(ifft(A.Ew));        % since we start with frequency
        , we need fftshift
141 A.ftt.Etdisp = A.Ewfft;                     % Get dispersed Et
142 A.ftt.tdisp  = linspace(A.t_w1,A.t_w2,A.N); % Get time axis
143
144 %In this function, inputting phi is only required to keep track of
145 %which was used. The code treats the ftt example has ALREADY HAVING
146 %DISPERSION - You can modify this code easily for yourself, but this
147 %was done to keep it simple!
148 A.ftt.PHITEXT = sprintf(['\\phi_0 = ', num2str(A.phi(1),'%.4g'),'\n',...
149 '\\phi_1 = ', num2str(A.phi(2),'%.4g'),'\n',...
150 '\\phi_2 = ', num2str(A.phi(3),'%.4g'),'\n',...
151 '\\phi_3 = ', num2str(A.phi(4),'%.4g'),'\n']);
152
153 otherwise
154 fprintf(2,'ERROR: The function FFTD did not complete, you did not enter a
        correct "type". Please use either ttf, ttt or ftt\n')
155 end
156 end
```